12-2011

An Investigation of Pinning Landscapes with Engineered Defects: Contact-free Critical Current Density Measurements

John William Sinclair
jsincla2@utk.edu

To the Graduate Council:

I am submitting herewith a dissertation written by John William Sinclair entitled "An Investigation of Pinning Landscapes with Engineered Defects: Contact-free Critical Current Density Measurements." I have examined the final electronic copy of this dissertation for form and content and recommend that it be accepted in partial fulfillment of the requirements for the degree of Doctor of Philosophy, with a major in Physics.

James R Thompson, Major Professor

We have read this dissertation and recommend its acceptance:

Hanno H. Weitering, Adriana Moreo, Janice L. Musfeldt

Accepted for the Council:
Carolyn R. Hodges

Vice Provost and Dean of the Graduate School

(Original signatures are on file with official student records.)

An Investigation of Pinning Landscapes with Engineered Defects:
Contact-free Critical Current Density Measurements

A Dissertation Presented for a
Doctor of Philosophy
Degree
The University of Tennessee, Knoxville

John William Sinclair
December 2011

ACKNOWLEDGEMENTS

I would first like to thank Dr. James R Thompson for all of the help and guidance that he has given me over these last 6 years. This would not have been possible without his wonderful ability to teach, his patience, and his knowledge. Secondly I'd like to thank my Father and Mother. Nothing I have done could have been done without them. These three people have made my adventure into graduate school possible.

Next I would like to thank Dr. David Christen for all of his help at Oak Ridge National Laboratory. He helped me so much in transitioning to Oak Ridge and away from being a full time class taker. I would also like to thank the rest of my committee: Dr. Moreo, Dr. Musfeldt and Dr. Weitering, for allowing me to take their time and giving their advice.

I would now like to thank the rest of my colleagues from my time at Oak Ridge National Laboratories: Özgür Polat, Ron Feenstra, Yuri Zuev, S. Cook, Fred List, Yifei Zhang, Nancy Ward and all of the rest of the people I worked and collaborated with during my time working at Oak Ridge. Working with them as been a delight and taught me a lot. Working with these people has made my time here very successful and fun.

Finally I want to acknowledge my wife Chelsea. Without her putting up with all of the late nights (especially near the end) and broken dates and being late for dinner, I do not think I would have made it to the finish line. Thank you so much!

ABSTRACT

Pinning landscapes in modern second generation coated conductors are excellent candidates for studies of vortex pinning. The ability to produce engineered defects in thin films of high temperature superconductors allows one to investigate representative distinct pinning sites, with the objective of understanding how different pinning centers contribute, compete and evolve under varying conditions of magnetic field strength and orientation, and temperature.

New contact-free methods were developed specifically to investigate this system in new ways, especially the dependence of the critical current density J_c on orientation of the magnetic field. A superconducting quantum interference device (SQUID)-based magnetometer was used to determine angular critical current density profiles. The induced currents produced in contact-free methods allow one to investigate a range of temperatures that is difficult to access by traditional transport measurements.

Materials with three distinctive pinning landscapes were investigated: Specifically, samples were studied that were dominated by columnar defects, by isotropic defects, or a mixture of these two types of pins. These studies over an expanded temperature-field-orientation phase-space clearly show competition between not only strong and weak pinning centers, but also between the angularly selective and nonselective pinning. This evidence is seen in critical current density profiles, the α [alpha]-values describing the falloff of J_c with magnetic field, and matching field effects in the three samples studied.

TABLE OF CONTENTS

LIST OF FIGURES

1 HISTORICAL REVIEW

The Materials

Superconductivity was first discovered by H. K. Onnes in 1911. He observed that when mercury was cooled below a critical temperature (T_c), the resistivity of mercury was reduced to zero[1]. He was able to observe this phenomenon because three years earlier he had discovered a method to liquefy helium, allowing him to study materials at very low temperatures. Mercury has a critical temperature of about 4 Kelvin, making the liquefaction of helium very important to this discovery. In the following years, many other elements and alloys were also shown to be superconducting, but the T_c's of these materials were all very low (well below 30 K). The materials studied in this thesis were discovered when a breakthrough in the materials came in 1986 when Bednorz and Muller discovered the cuprate superconductors[2]. These materials were not alloys but rather layered perovskite-related cupric oxide materials. The initial material that they discovered was lanthanum barium copper oxide with a critical temperature of 35 K. Within a year, many more materials had been discovered, many of which had critical temperatures above 77 K (which is technologically important due to it being the normal boiling point temperature of liquid nitrogen). Later in 2008 iron-based superconductors were discovered[3].

In this dissertation we will specifically study thin film superconductors, many of which have wire applications. Specifically we will be studying high-T_c cupric oxide thin films, with most synthesized by chemical deposition (MOCVD) on ion beam assisted deposition (IBAD) substrates[4] and most of them will be 2G superconducting wire or

coated conductor (CC) made by SuperPower Inc[5]. There is a strong metallic substrate to provide strength and flexibility followed by insulating buffer layers. The insulating buffer layers provide both (1) chemical stability between the metallic substrate and the superconducting thin-film that is at the top of the wire and (2) an epitaxial template for growth of a highly textured film.

The Meissner Effect

In 1933, W Meissner and R Ochsenfeld discovered that a superconductor is fundamentally different from a perfect conductor. Their discovery can be succinctly stated as a superconductor will expel weak magnetic fields even if the magnetic field is static[6]. In 1935 the London brothers proposed a set of equations that theoretically explain the Meissner effect[7]. Equations 1.1 and 1.2 are the relations that the London brothers developed to describe this phenomenon.

$$\frac{dJ}{dt} = \frac{n_s e^2}{m} E \tag{1.1}$$

$$\nabla \times J = -\frac{n_s e^2}{mc} B \tag{1.2}$$

Using equation 1.2 and Maxwell's equations, one can isolate the magnetic field *B* and solve a simple differential equation to understand how *B* varies in the sample. Equation 1.3 shows the differential equation and equation 1.4 is the solution for the

simple geometry of a semi-infinite slab with its surface at $x = 0$ in the presence of a magnetic field applied parallel to the surface.

$$\vec{B} = -c\vec{\nabla} \times \vec{\nabla} \frac{4\pi n_s e^2}{mc^2} \vec{B} \rightarrow \nabla^2 B = \frac{1}{\lambda^2} B \quad (1.3)$$

$$B(x) = Be^{-\lambda x} \quad (1.4)$$

In equations 1.3 and 1.4, λ is a constant, called the London penetration depth, defined as $\lambda = \sqrt{\frac{mc^2}{4\pi n_s e^2}}$ and x is the distance into the superconductor. The flux density within the superconductor vanishes exponentially fast with distance, even if the external magnetic field is constant; this result is consistent with the experimentally observed Meissner effect.

Ginzburg-Landau Theory

In 1950, Lev Landau and Vitaly Ginzburg developed a phenomenological macroscopic model in an effort to study superconductivity by using the theory of second order phase transitions[8]. This theory, known as Ginzburg-Landau theory of superconductivity (or GL theory), proposed a complex pseudo-wavefunction ψ that acts as the order parameter and is formulated such that $n_s = |\psi|^2$ where n_s is the number density of superconducting electrons.

Near T_c, the free energy of the superconductor can be expanded in a power series as a function $|\psi|^2$. Assuming that ψ is varying slowly in space, the free energy near T_c can be written as equation 1.5.

$$f_s = f_n + \alpha|\psi|^2 + \frac{\beta}{2}|\psi|^4 + \frac{1}{2m^*}\left|\left(\frac{\hbar}{i}\nabla - e^*\vec{A}\right)\psi\right|^2 + \frac{H^2}{8\pi} \quad (1.5)$$

In the absence of fields and gradients (the spatially uniform case), equation 1.5 reduces to equation 1.6.

$$f_s - f_n = \alpha|\psi|^2 + \frac{\beta}{2}|\psi|^4 \tag{1.6}$$

If one minimizes equation 1.6 with respect to $|\psi|^2$, one obtains the condensation energy as seen in equation 1.7.

$$f_s - f_n = \frac{\alpha^2}{2\beta} = -\frac{H_c^2}{8\pi} \tag{1.7}$$

In equation 1.7, H_c is the thermodynamic critical field. Ginzburg and Landau then minimized the more general free energy using a variational principle and derived a differential equation for ψ and a corresponding equation for the supercurrent density *J*. These are described in equations 1.8 and 1.9, respectively.

$$\alpha\psi + \frac{\beta}{2}|\psi|^2\psi + \frac{1}{2m^*}\left(\frac{\hbar}{i}\nabla - e^*\vec{A}\right)^2\psi = 0 \tag{1.8}$$

$$\vec{J} = \frac{e^*\hbar}{2m^*i}(\psi^*\nabla\psi - \psi\nabla\psi^*) - \frac{e^{*2}}{m^*c}|\psi|^2\vec{A} \tag{1.9}$$

GL theory also introduces two new length scales. The first length scale is the coherence length ξ.The coherence length is the characteristic length over which ψ can vary without large energy increases and equation 1.10 is how it is defined.

$$\xi(T) = \frac{\hbar}{|2m^*\alpha(T)|^{1/2}} \tag{1.10}$$

They also defined a new temperature dependent penetration depth $\lambda(T)$ which is logically consistent with the more phenomenological length scale introduced by the Londons and is defined in equation 1.11.

$$\lambda(T) = \sqrt{\frac{m^*c^2}{16\pi e^{*2}\psi_0^2}} \tag{1.11}$$

Since $\xi(T)$ and $\lambda(T)$ diverge in the same way as T_c is approached, one can define the GL parameter κ that is dimensionless and approximately temperature independent. This parameter is defined as the ratio of the penetration depth and coherence depth $\kappa = \frac{\lambda(T)}{\xi(T)}$.

2 INTRODUCTION TO THEORY ELEMENTS

Type-I and Type-II Superconductivity

The Ginzburg Landau parameter κ will define two fundamentally different types of superconductivity, type-I and type-II. The difference between the two types of superconductors is their behavior in the presence of a magnetic field. In small magnetic fields, both type-I and type-II superconductors have a Meissner state behavior, but in the presence of large magnetic fields, type-II superconductor allows flux to enter as quantized vortices[9].

A type-I superconductor is one in which the Ginzburg Landau parameter is $\kappa < \frac{1}{\sqrt{2}}$. . A type-I superconductor, in the presence a magnetic field, will have a Meissner state up to the thermodynamic critical magnetic field H_c. Above this magnetic field, the superconductor is driven into its normal state. This provides a temperature-magnetic field phase space in which the material is either in a superconducting Meissner state or a normal state. This is qualitatively shown in figure 1 a.

When the Ginzburg Landau parameter is $\kappa > \frac{1}{\sqrt{2}}$, the superconductor is a type-II material. A type-II superconductor has a more complicated temperature-magnetic field phase space, as can be seen in figure 1 b. Again for small applied magnetic fields the superconductor is in a Meissner state. Above a lower critical field, H_{c1}, magnetic flux begins to enter the superconductor. This state is known as the mixed state or vortex state. The magnetic flux enters the superconductor as quantized vortices where the flux

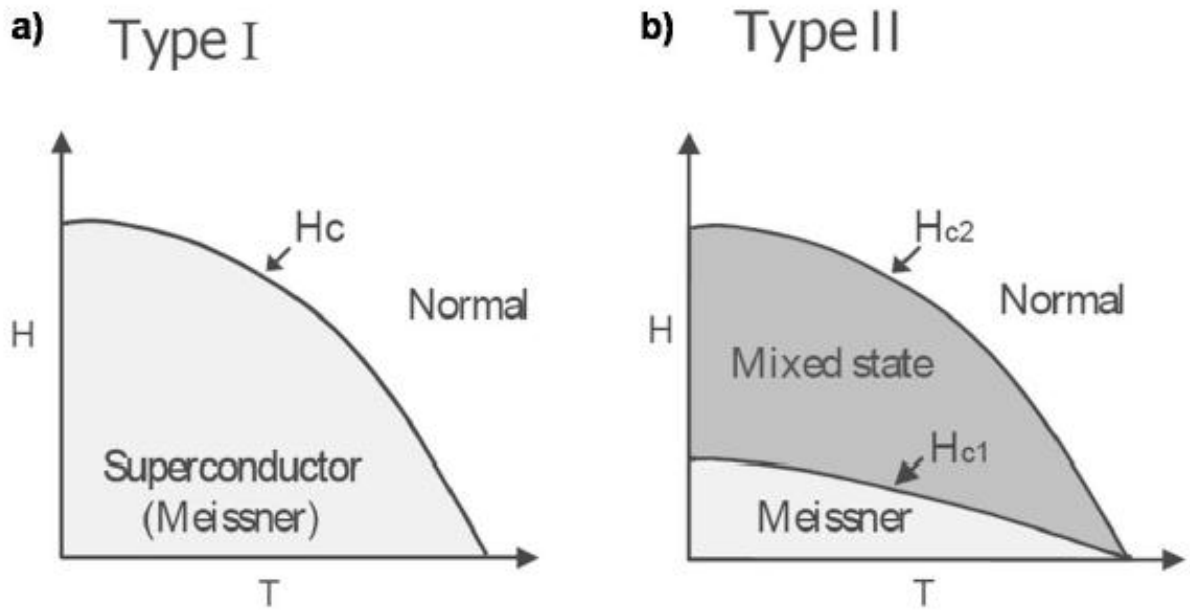

Figure 1: a) Shows a type-I superconductor with only a Meissner state and a normal state. b) Shows a type-II superconductor that has a Meissner state below H_{c1} and a mixed or vortex state above H_{c1} and below H_{c2} and a normal state above H_{c2}.

quantum is $\Phi_0 = \frac{h}{2e}$. The vortex has currents circulating in a profile with a radius of order λ and a core that is of order ξ in radius. Figure 2 has a schematic depicting a vortex. In this thesis, type-II superconductors will be studied exclusively. Once magnetic flux begins to enter the superconductor, there are several new phenomena that occur in the superconductor.

Vortices

Vortices will enter the superconductor and form a lattice of magnetic flux,[10] assuming only intervortex interactions are important. In the presence of an imposed electric current density *J*, the Lorentz force density ($F_L = J \times B$) will cause the vortices to move at velocity *v* that is limited by the effective viscous drag in the superconductor. This vortex motion will induce an electric field as can be seen in equation 2.1.

$$\vec{E} = -\vec{v} \times \vec{B} \tag{2.1}$$

The vortex motion will be perpendicular to the current density and the magnetic field as is depicted in figure 3, meaning that **E** is parallel to **J**. Once an electric field is induced, a power loss per unit volume will exist as shown in equation 2.2.

$$P = \vec{E} \cdot \vec{J} \tag{2.2}$$

This power loss is due to the motion of the vortices. If it is possible to reduce the velocity of the vortices by pinning them in place, then the power dissipation will be reduced. To achieve this, one must create potential barriers that keep the vortex motion to a minimum.

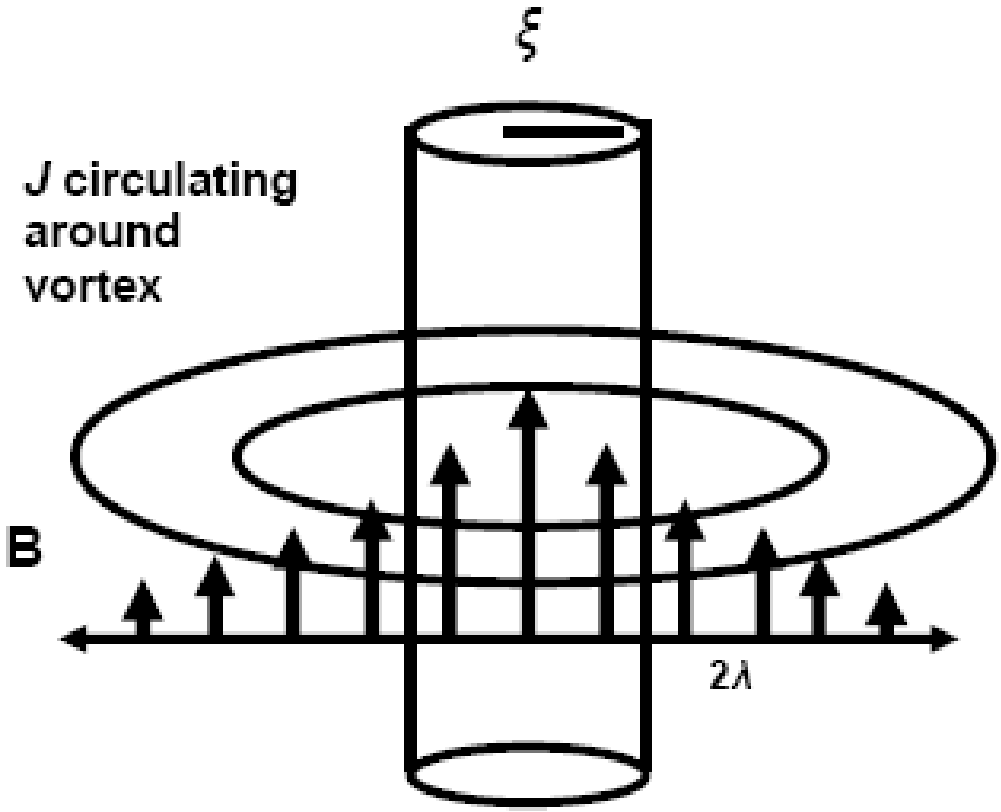

Figure 2: A schematic depiction of a typical vortex. Currents, like winds in a tornado, circulate around a vortex core. The winds extend outward to a distance of order λ and the vortex core is of order ξ in radius.

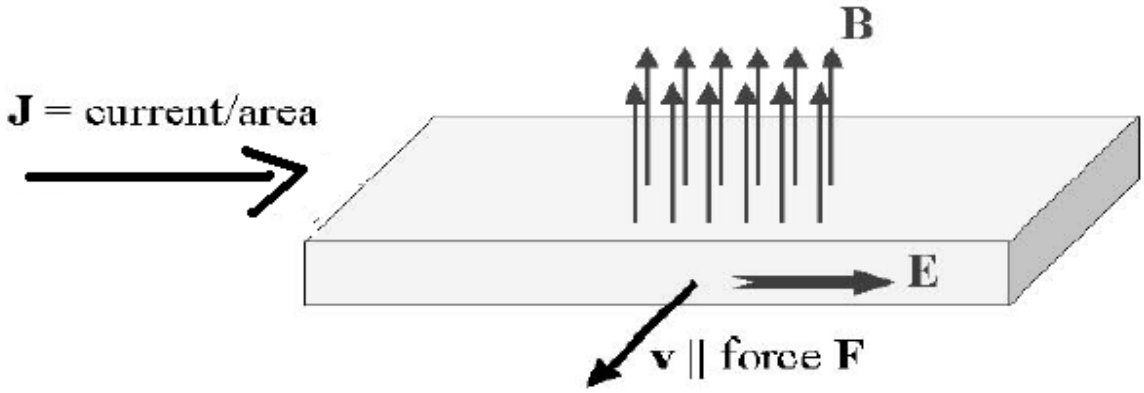

Figure 3: Schematic showing relevant vector directions for a type-II superconductor in the mixed state in the presence of an applied magnetic field.

Pinning Vortices

The first flux that enters a type-II superconductor enters as a single vortex. As the applied field increases, so does the number of vortices. As long as the spacing of the vortices is large compared to the penetration depth it is possible to ignore vortex-vortex interactions. When these conditions are met, the free energy per unit length for the vortex line (ϵ_1) is given by equation 2.3[11].

$$\epsilon_1 \approx \left(\frac{\Phi_0}{4\pi\lambda}\right)^2 \ln\left(\kappa + {}^1/_2\right) = \frac{H_c^2}{8\pi}\xi^2 \ln\left(\kappa + {}^1/_2\right) \qquad (2.3)$$

Equation 2.3 relates the free energy of the vortex line to the square of the coherence length. This relation implies that defects in superconductors that are not superconducting present an energetically favorable position and can pin the vortex (by regaining the vortex core energy). There are many different types of pinning that will be

discussed in this thesis, but fundamentally they all provide an energetic barrier for the vortex to overcome to prevent the motion of the vortex.

The motion of a vortex experiencing a Lorentz force is the origin of the dissipation in superconductors. To minimize this dissipation, a pinning force density, $\boldsymbol{F_P}$, must exist that is at least equal to the Lorentz force. When the applied force is equal to the maximum available pinning force, the current density producing that force is the critical current density (J_c). The pinning force density is an important parameter and is related to the critical current density as seen in equation 2.4.

$$J_c \equiv {}^{F_p}/_{B} \tag{2.4}$$

Types of Pinning

Vortices can be pinned in many ways. Starting with equation 2.3, if a superconductor is anisotropic there will be intrinsic pinning because ξ is inversely proportional to the square root of effective mass of the electrons, which will be discussed further in the next section. Secondly, nonsuperconducting material can be introduced into the superconducting matrix by various means to pin the vortices. For example, superconducting materials have been irradiated by energetic heavy ions; this generates columnar pinning sites as the radiation penetrates the sample producing amorphous tracks that increase pinning and decreases flux creep[12]. Also the presence of this type of defects has been shown to increase the irreversibility line, which is also evidence of increased pinning[13]. More recently, microscopic nonsuperconducting regions have been formed in the superconductor during the synthesis process, e.g., as second phase precipitates or

strain fields. This allowed one to introduce columnar or isotropic pinning sites to even large scale processes[14, 15].

Intrinsic pinning

In the materials that are studied in this thesis, there is enough anisotropy due to their layered nature to produce noticeable pinning effects. The layered oxide materials have strong superconductivity in the CuO planes and are weakly linked in the *c* direction. The layered nature of these materials is illustrated in figure 4 (a diagram of $YBa_2Cu_3O_7$ which is the cuprate that is mainly studied in this thesis). If a magnetic field is applied in the *ab* plane, the vortices will try to form in the layered structure. In this direction the superconducting order parameter is modulated by the layered crystal structure, as well as the condensation energy. A Lorentz force in the *c*-direction would try to force the vortices to move from *ab* plane to *ab* plane, which is much more difficult, making the intrinsic anisotropy a powerful pinning force in cuprates[11].

Extrinsic Pinning

Heavy ion irradiated high T_c cuprates were the first samples with extrinsic columnar strong pinning centers. These studies showed the possibility of strong extrinsic pinning centers with a "tailored" geometry. If one were to consider the angular critical current density of a sample with linear columns created by heavy ion irradiation, it would be angularly selective. There would be a peak in the current density when the applied magnetic field is aligned with the column-like pins. When this condition is met, the vortex is most optimally pinned by pinning the whole length of the vortex. Other types

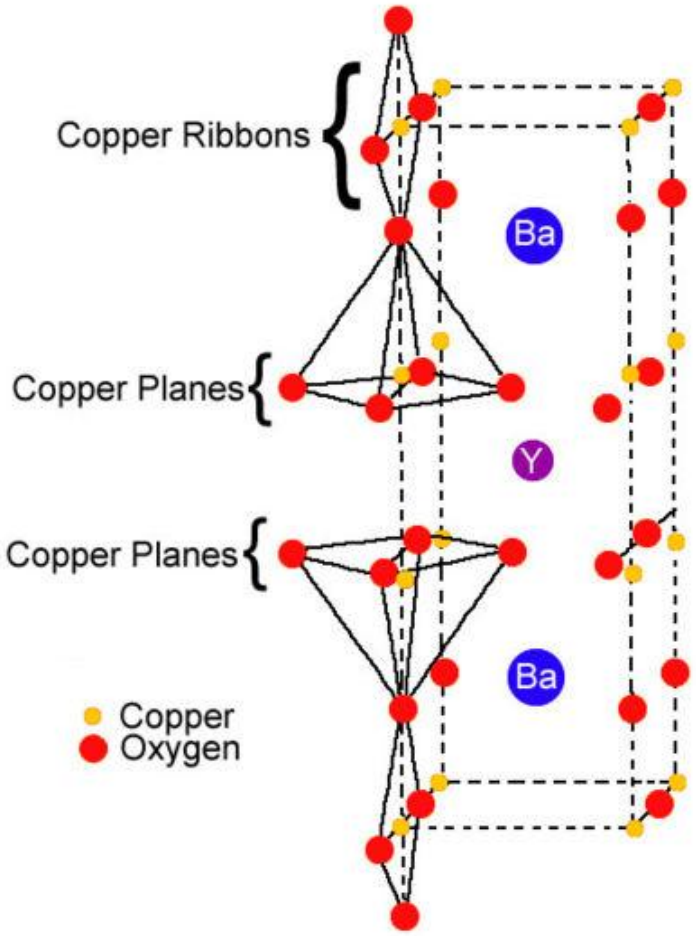

Figure 4: A schematic figure of the structure of YBCO. There is strong superconductivity in the CuO planes and weak coupling between CuO-CuO planes.

of irradiation were used early on as well to create isotropic pins. Bugoslavsky et al. used protons to create a nearly isotropic angular current density in MgB_2 for example[16].

Later, defects were engineered by introducing oxide materials and second phase rare earth oxides that will act as pinning centers. Different materials will form isotropic pins and others will form correlated disorder such as columns. Adding second phase rare earth oxides will introduce large isotropic pins centers that produce strong pinning. Consequently pins of an isotropic nature will add no extra angular dependence, meaning that the electronic anisotropy determines the angular profile. Adding other materials such as $BaSnO_3$ or $BaZrO_3$ can create columnar defects. These pinning centers will have angularly selective pinning. This allows one to synthesize a material that is either dominated by isotropic pinning or correlated disorder or a mixture of both. This should produce many unique and interesting properties in the pinning landscape.

Figure 5 shows a cartoon of engineered isotropic pins. In reality these pins are mostly isotropic and are randomly dispersed in the superconducting matrix. The pinning produced by this defect would be by itself angularly independent; consequently, the current density profile of a sample dominated by this type of pinning depends only on the effective mass anisotropy: $\gamma = \sqrt{m_c/m_{ab}}$ (where $\gamma \approx 5$). Blatter et al. have shown that in the case of isotropic pins that $J_c(H,\theta) = J_c(\tilde{H})$ where $\tilde{H} = \varepsilon(\theta)H$ and $\varepsilon(\theta) = \sqrt{\cos^2\theta + \gamma^{-2}\sin^2\theta}$; this produces a minima in the angular critical current density profile at $\theta = 0$ (assuming J_c decreases with H, as is usually the case)[17].

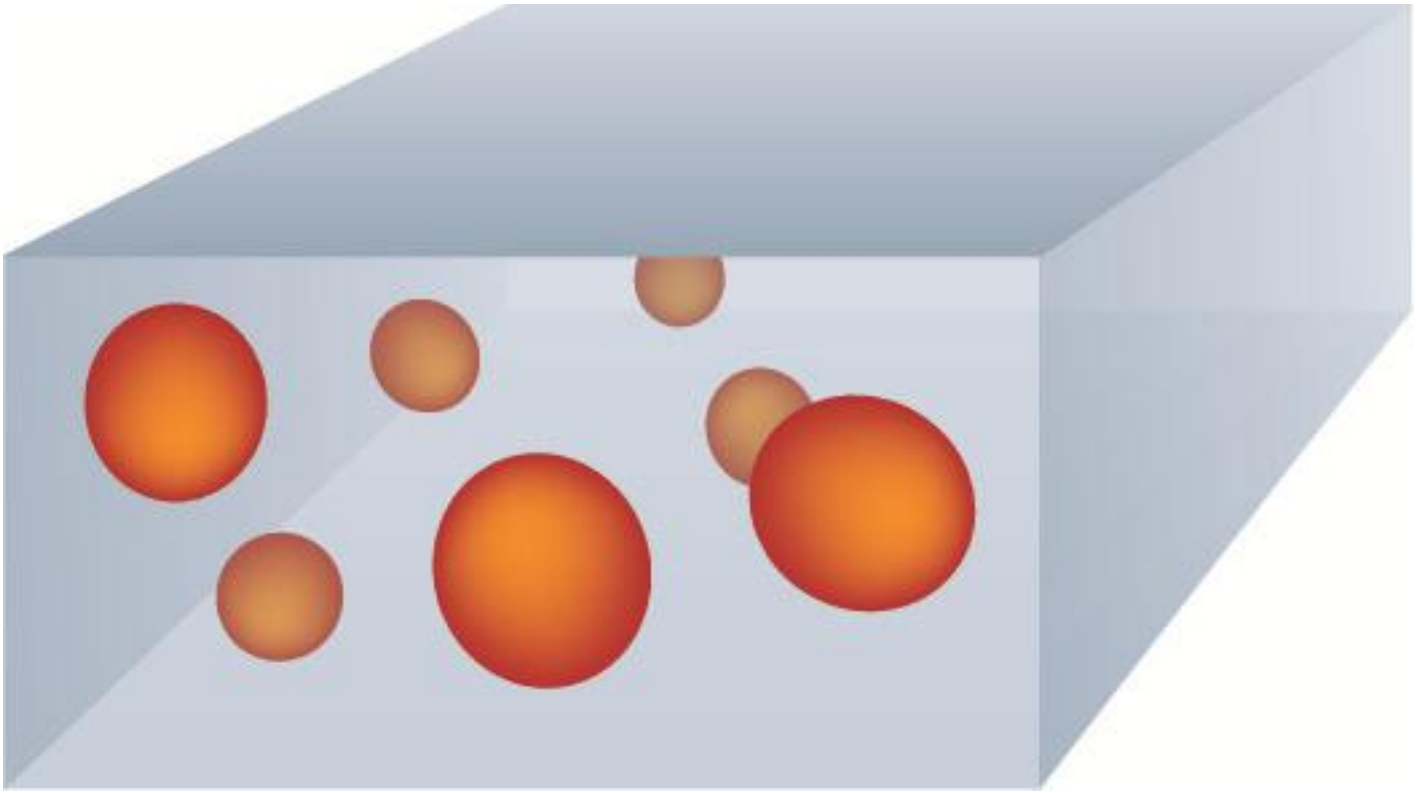

Figure 5: Isotropic pins (here colored yellow) are nonsuperconducting materials randomly dispersed in a superconducting matrix (here colored blue). The pinning produced by these pins is not angularly selective.

Figure 6 shows a cartoon of engineered correlated pins, comprised of a stack of nanodisks of second phase material. These pins can form when a newly added nanodisk senses the location of previous nanodisks, through the lattice mismatch and strain field that result from deposition of the material. As the material is formed layer-by-layer, the nanodisks will align causing columns to form. Materials such as $BaZrO_3$ and $BaSnO_3$ are common materials to form columnar defects. Much like the irradiated samples, samples dominated by correlated disorder will have a peak in the current density when the vortices in the material align with the columnar pins.

Modeling Behavior of Critical Current Densities

In the above section, a qualitative and intuitive understanding of the types of disorder that can be introduced into the superconducting matrix was presented. An interesting phenomenon for study is the temperature dependence of the critical current density of a superconductor with various mixtures of different types of pins. To do this, one must know the temperature dependence of different strengths of pinning.
A logical starting point to begin to understand the temperature dependence of different types of pinning is by studying current density decay in the presence of an applied magnetic field.

Anderson and Kim in 1962 and 1964 published important work in the study of vortex motion creating current decay. Their theory describes a situation in which vortices move because of thermally activated hopping from one pinning site to the next. Their

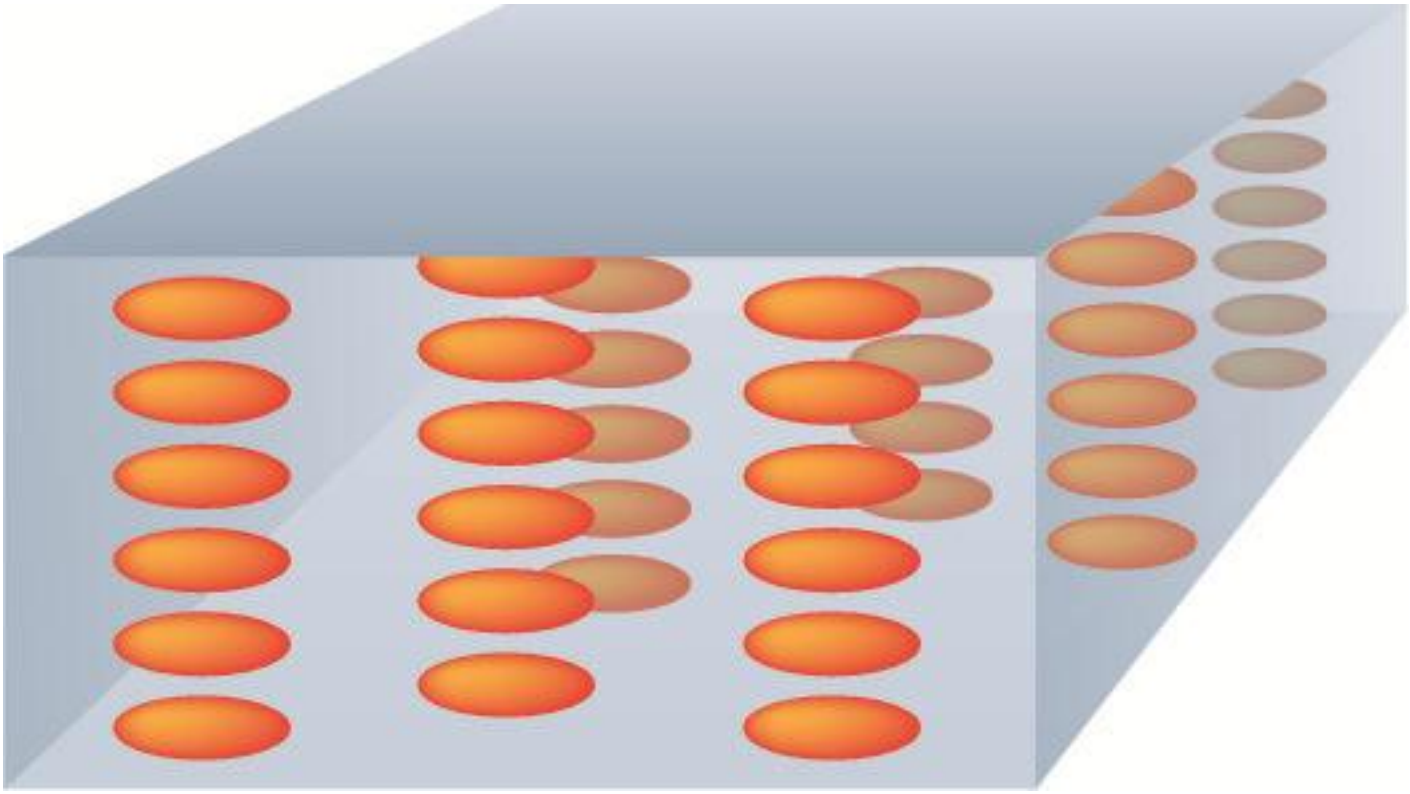

Figure 6: Columnar pins (here colored yellow) can be grown in a superconducting matrix (here colored blue).These pins will optimally pin vortices when the applied magnetic field is aligned with the pins. The current density will be peaked when this condition is met.

work resulted in an understanding of the time decay of critical current densities of type-II superconductor[18 19]. Blatter et al. succinctly illustrates many different theories for understanding creep[11]. When measurements are made in a magnetometer, a relatively long time passes between the initial induced currents and the currents one is measuring. Also one is measuring a current density that is much less than the critical current density ($J << J_c$). When these conditions are met, Blatter et al. proposes a current density as a function of time relations that is shown in equation 2.5.

$$J(t) = J_c e^{-\frac{T}{U_c}\ln\frac{t}{t_0}} \quad (2.5)$$

The symbols in equation 2.5 are as follows: *J* is the current density, *T* is the temperature, U_c is the collective pinning energy, *t* is the time, t_0 is the average attempt time it takes a vortex to hop from one pinning site to another. As a consequence of equation 2.5, there is an interesting temperature dependence that can be inferred at time *t*. This relation can be described by equation 2.6[11].

$$J(T) \simeq J_c(0) e^{-\frac{T}{T_0}} \quad (2.6)$$

The relation shown in equation 2.6 does not take into account any correlated nature of the pins, so one would associate this form of temperature dependent current density evolution with isotropic or weak pins.

Nelson and Vinokur developed a theory for columnar defects in 1993. They estimated a columnar defect as a cylindrical quantum well of depth U_0 and radius c_0. Using these quantum wells, they solved the London and Ginzburg and Landau equations to determine U_0 and the critical current densities. They then took thermal fluctuations into account to give the temperature dependence seen in equation 2.7.

$$J_c(T) \simeq J_c(0)e^{-3(T/T^*)^2} \quad (2.7)$$

Equation 2.7 uses a term T^* which is a temperature related to the energy scale of the pins in question.

In 2002, Plain and colleagues wanted to study the effects of microstructure of superconductors on the temperature dependence of the critical current density. They chose to sum equations 2.6 and 2.7 to produce equation 2.8 as a good first approximation of the temperature dependence of a more complicated mixed pinning landscape[20].

$$J_c(T) \simeq J_c^{wk}(0)e^{-T/T_0} + J_c^{str}(0)e^{-3(T/T^*)^2} \quad (2.8)$$

This gives one an analytical tool to help judge which type of pinning is dominant for a given sample in some temperature range.

3 EXPERIMENTAL METHODS

A magnetometer, based on a superconducting quantum interferometer device (SQUID), was used to investigate the J_c of second generation (2G) superconducting wires and other superconducting thin films. The SQUID device was used to determine the magnetic moment of the superconductor and from the irreversible magnetization of the sample determine the J_c. One may employ the Bean critical state model to determine the J_c of the investigated materials. This method of investigating J_c is a contact-free measurement that has many advantages over traditional transport measurements. Because the method is contact-free, it allows us to increase not only the temperature phase space investigated, but also the electric field phase space. Because of the induced electric field, a power loss occurs as was explained earlier in chapter 2. Due to this power loss, we also will use SQUID magnetometry to investigate J_c as a function of time to study the decay of the current density. Lastly, we improved our contact-free methods by developing a way to extend this method to angular current density studies, i.e., for different orientations of the applied magnetic field. This is achieved by using both a longitudinal and a transverse SQUID pick-up coil in the same MPMS to determine the longitudinal and transverse magnetization, which is oriented parallel and perpendicular to the applied field, respectively.

SQUID Magnetometry

The magnetic measurements in this study were performed with a SQUID –based magnetometer. These instruments are very sensitive to changes in magnetic flux (a fraction of a flux quantum). We used a commercially available device from Quantum

Design Inc. It is a magnetic properties measurement system (MPMS) with a 7 tesla magnet. The model is a MPMS-7. The smallest magnetic moment the MPMS-7 can measure is ~10^{-7} emu and an extended range option allows measurements to 300 emu. At the center of the magnet, the magnetic field is uniform to within 0.01% over a 4 cm axial distance. The lowest temperature achievable is 1.9 K with an accuracy of 0.01 K.

Figure 7 is a schematic drawing of a SQUID magnetometer. The SQUID device itself uses the principle of Josephson junctions[21]. A superconducting ring with one or two thin insulating layers, creating weak links to form parallel Josephson junctions, comprises the main component of the SQUID sensor. If a constant bias current is maintained in the SQUID, the measured voltage will oscillate with the changes of phase in the two junctions. This phase change is directly related to the change in magnetic flux. The measured voltage and instrument sensitivity are calibrated by using samples that have a known magnetic moment, such as a Ni sphere or Pd metal susceptibility standard. Once the instrument has been calibrated, the measured induced voltages can then be used to accurately measure magnetic moments of unknown samples. The sample is mounted on a sample rod and centered between a set of detection coils that are coupled to the SQUID sensor by superconducting wires.

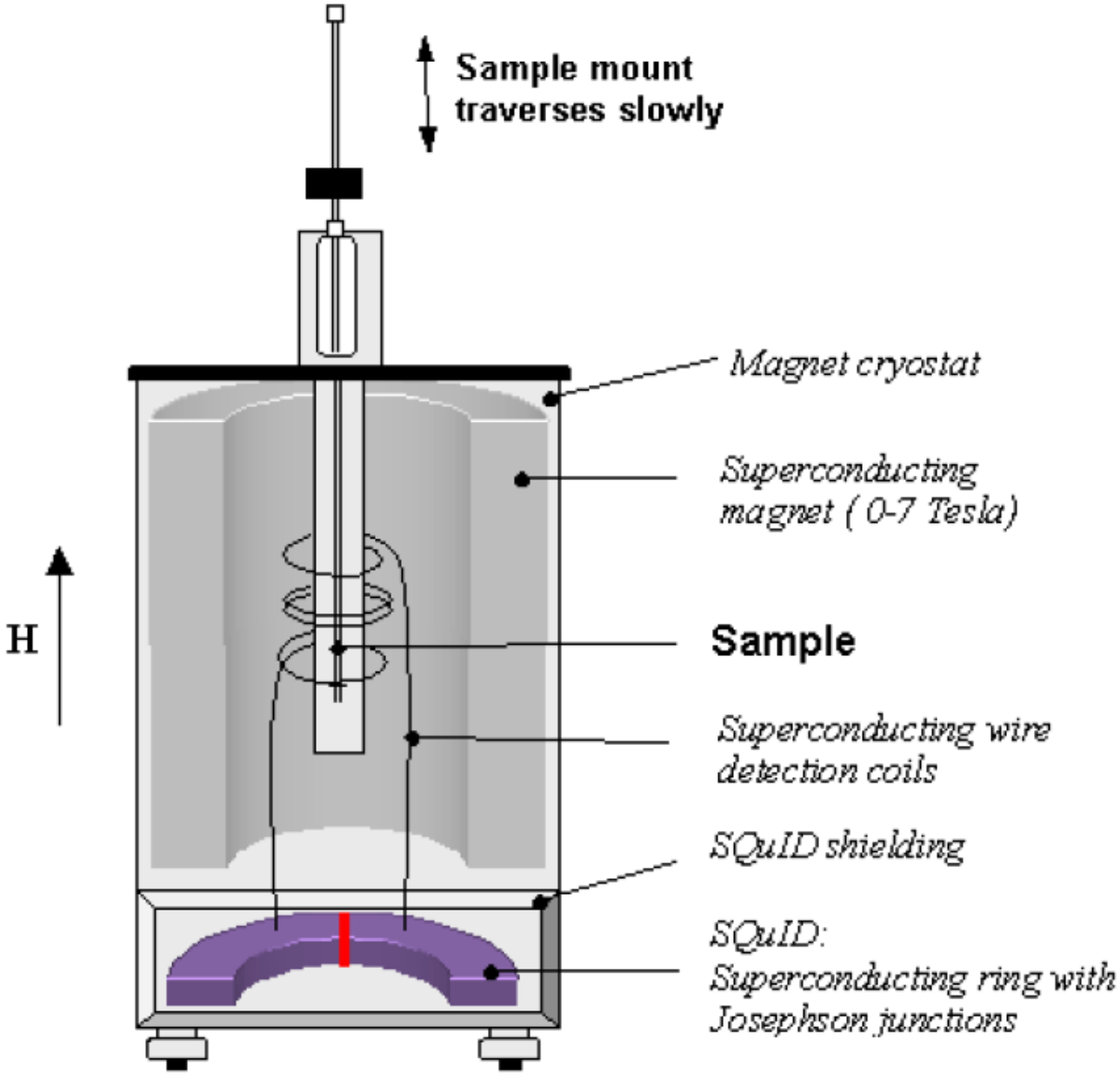

Figure 7: A schematic drawing of an MPMS system using a SQUID sensor.

The system of detection coils and superconducting wires form a dc flux transformer that helps reduce the problems of external fields. It is a continuous superconducting wire that is wound to form a transformer at one end and as a second-derivative coil in the sample space, as one can see in figure 8.

The longitudinal pickup coil has three sections. The top and bottom sections each have a coil wound in a clockwise sense and the middle section is a coil with two turns wound a counterclockwise manner. With this second-derivative configuration, the pickup (sample detection) coil is insensitive to a uniformly varying magnetic field, but it is sensitive to a magnetic moment that is translated through it. The resulting output voltage from the SQUID detection system is then compared to and fit to the scan pattern produced by a perfect dipole.

Bean Critical State Model

The Bean critical state model allows one to determine the critical current density (J_c) from the irreversible magnetization induced in a superconducting sample. This theory begins by supposing a current is induced by a changing magnetic field, applied perpendicular to a superconducting sample, by Faraday's law. The current flows according to Lenz's law to oppose the change in flux due to an applied magnetic field. Next Bean proposes two major assumptions to theoretically understand hysteresis in type-II superconductors. The first fundamental assumption of this model is that the magnetization, *M*, will vary linearly through a superconducting slab of thickness *D* and all changes in the flux distribution are induced at the sample surface. The second

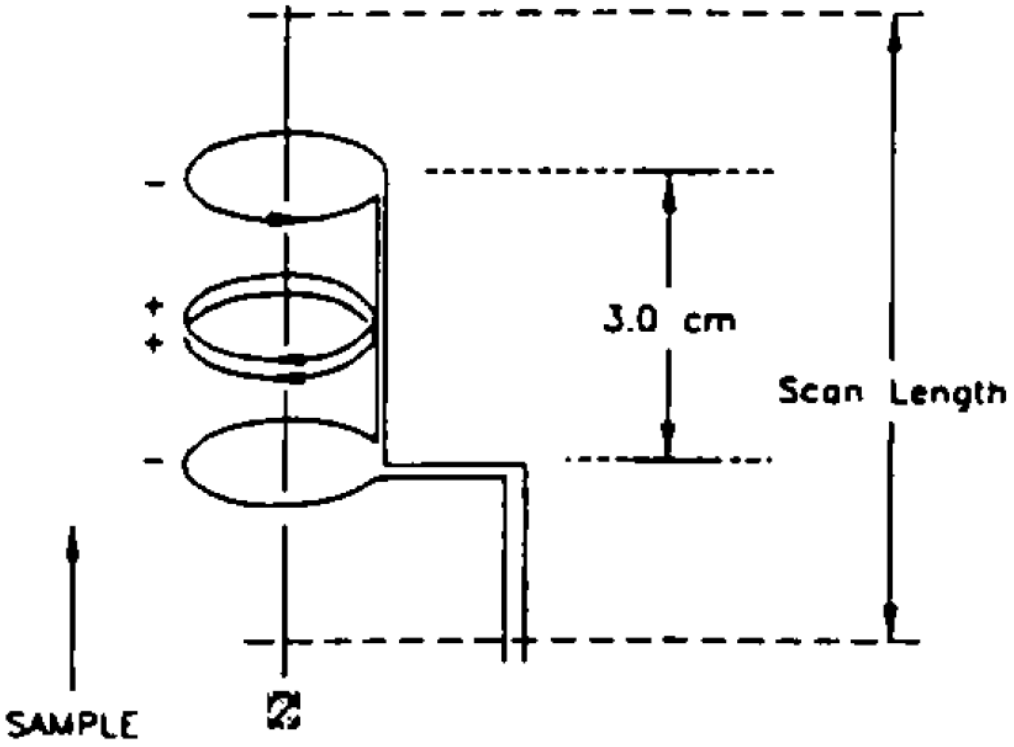

Figure 8: An illustration of a flux transformer. The second-derivative coil geometry is in the sample space.

assumption is that the presence of even the smallest electromotive force will produce only one current density, specifically the critical current density. This simplest form of the model is valid only when the sample is fully penetrated. This occurs above some applied field, *H*, resulting in a finite field everywhere in the sample interior. We call this applied magnetic field H^*. Figure 9 illustrates these assumptions and shows cases where the sample is fully penetrated and partially penetrated[22, 23].

If one then starts with the most basic definition of a magnetic moment of a dipole, equation 3.1, and use these assumptions, one can infer the J_c from the magnetic moment *m*.

$$m = \frac{1}{2}\int r \times J \, dV \tag{3.1}$$

If we then use the assumptions of the Bean critical state model, one can extract the current density. Equation 3.2 is the Bean critical current density for a cylinder with radius *r* in SI units.

$$J_c = \frac{3\Delta M}{r} \tag{3.2}$$

Here $\Delta M = M^- - M^+$ is the change in the irreversible magnetization for the decreasing and increasing applied field histories, where $M = {}^{m}/_{volume}$. The samples that are investigated in this study are not cylinders, but rather are rectangular slabs or thin rectangular strips. In this particular geometry, a rectangle with sides $b>a$, equation 3.3 gives one the J_c using the sandpile model.

$$J_c = \frac{20\Delta m}{V}\left(a\left(1 - \frac{a}{3b}\right)\right)^{-1} \tag{3.3}$$

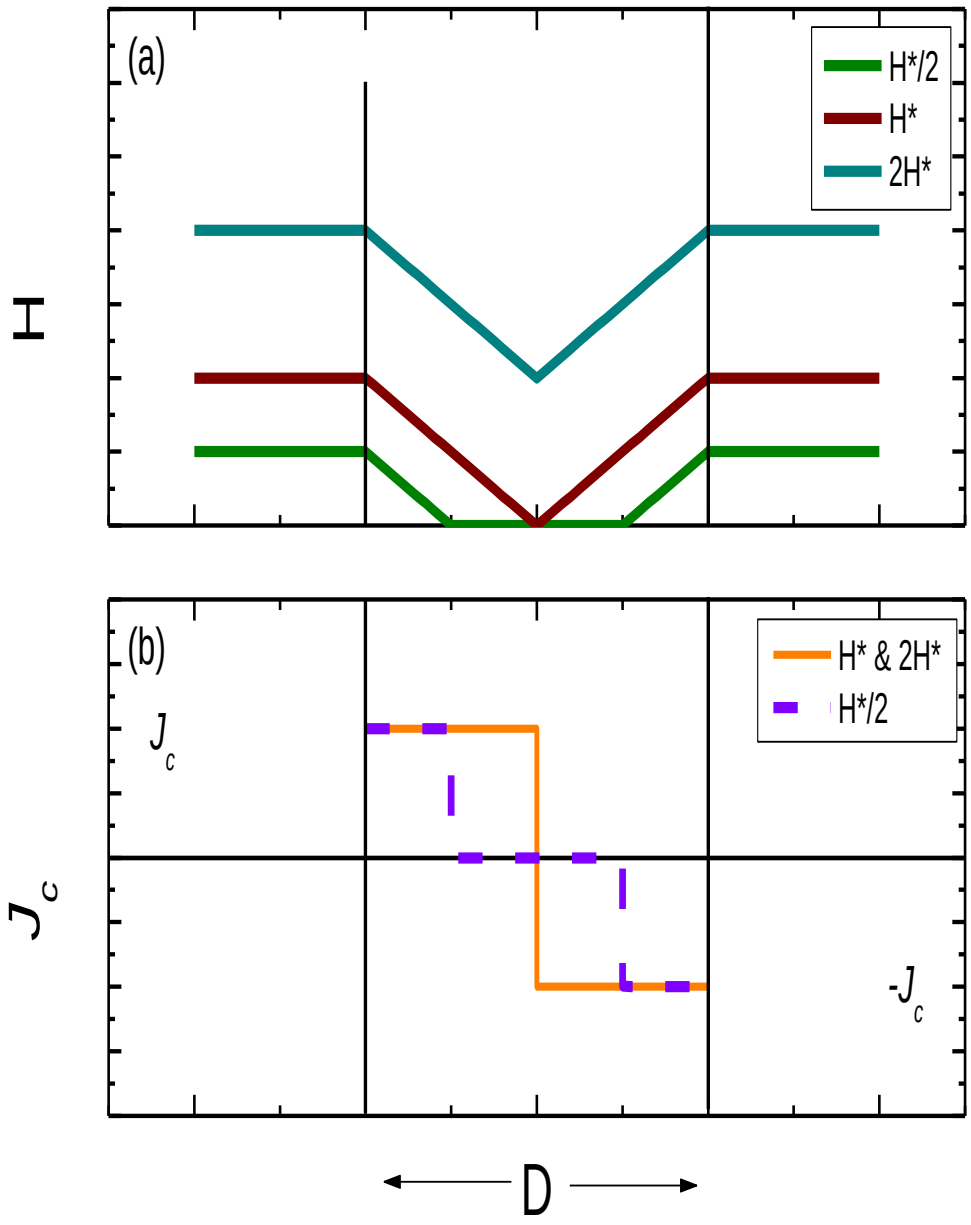

Figure 9: In this figure we have the magnetic field profile (a) and the J_c (b) as a function of distance into the superconducting slab. This figure assumes that initially, no currents flow in the superconductive slab and the magnetic field increases monotonically.

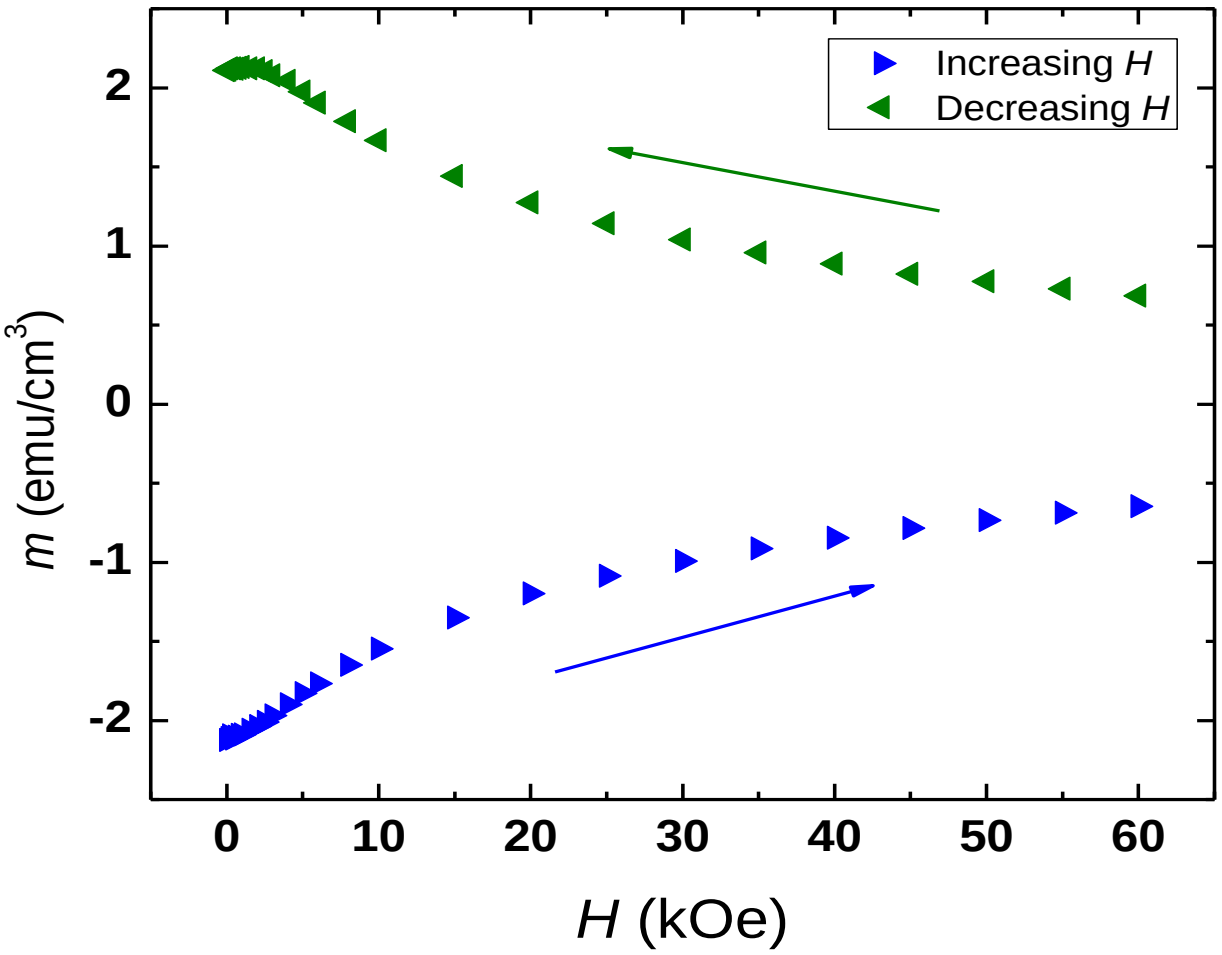

Figure 10: A typical hysteresis loop of an already fully penetrated sample provides the irreversible magnetic moment to be used to determine the J_c in the Bean critical state model. We have both the increasing and decreasing branches of the hysteresis loop.

This new effective radius (transverse dimension) is called the “sandpile radius” and is effectively the largest inscribable ellipse in a rectangular sample[24].

One may now use a SQUID magnetometer to measure a hysteresis loop at various temperatures to determine the field and temperature dependence of J_c in a superconductor. A typical hysteresis loop can be seen in Figure 10. From the hysteresis loop, one can determine the irreversible magnetization and then by using equation 3.3 determine the J_c. Lastly one must take care to ensure that the sample is fully penetrated before make a hysteresis measurement, because only once the sample is fully penetrated is equation 3.3 valid.

Contact-Free Method

Since the current density of a sample can be inferred from a hysteresis loop, this method does not require contacts to be attached to a sample to produce a voltage difference between the ends of a sample. There are many advantages to this type of measurement. Chief among these reasons is that the induced currents tend to have self-limiting dissipation levels. Due to self-limiting dissipation levels from the induced currents, we can also study samples at lower temperatures and all available applied magnetic field ranges without the fear of destroying (burning out) the sample.

Induced currents and self-limiting dissipation levels are the most important difference between contact-free methods and traditional four point probe methods. In traditional transport measurements this problem is solved by patterning the sample into narrow gates or by only studying the samples at relatively high applied magnetic fields where the current densities will not be too high. If too much current is forced through the

sample and the dissipation levels are not self-limiting, you can destroy your sample. Using contact-free methods, one can easily complement transport measurements at the traditional 77 K and 65 K by expanding the temperature range down to 5 K at all available applied magnetic fields.

Electric Field Criterion

Because the level of electric field is not simply imposed with contact-free methods, one must find a way to determine the effective electric field that is induced by the current decay over time. The electric field averaged over the perimeter for rectangular samples (with sides $a<b$ and thickness $d<<a$) can be calculated as follows, remembering the demagnetization factor (D) is important for our thin film geometry. First we define the average electric field of the perimeter ($\langle E_{perm} \rangle$ in equation 3.4.

$$\langle E_{perm} \rangle = \frac{1}{2(a+b)} \frac{d\Phi_B}{dt} \tag{3.4}$$

Next one must find Φ_B. To do this, one uses the definition of the critical current density in the sandpile model. We then invert equation 3.4 solving for M and producing 3.5. Here we use a new definition of the sandpile model assuming that $\Delta M = 2M$. Equation 3.5 solves for M in SI units.

$$M = \frac{a\left(1-\frac{a}{3b}\right)}{4} J_c \tag{3.5}$$

Now we can relate M to B to determine Φ_B. Again remembering the importance of the demagnetization factor, equation 3.6 gives one the magnetic field B

$$B = \mu_0\left(H_{eff} + M\right) = \mu_0(H_a - DM + M) = \mu_0 H_a + (1-D)\mu_0 M \tag{3.6}$$

Now we can calculate Φ_B using equations 3.5 and 3.6 as is seen in equation 3.7.

$$\Phi_B = B \cdot A = \mu_0 H_a ab + ab(1-D)\mu_0 M = \mu_0 H_a ab + ab(1-D)\mu_0 \frac{a}{4}\left(1 - \frac{a}{3b}\right) J_c \quad (3.7)$$

Now we must calculate the demagnetization factor. Using some simple algebra and that $d<<a<b$ one can calculate 1-D as shown in equation 3.8.

$$1 - D \approx \frac{d}{a} \quad (3.8)$$

Finally we can now calculate $\langle E_{perm} \rangle$ as seen in equation 3.9.

$$\langle E_{perm} \rangle \approx \frac{a^2 bd\left(1-\frac{a}{3b}\right)\mu_0}{8(a+b)a} \frac{dJ}{dt} = \frac{1}{8}\mu_0 da \frac{dJ}{dt} \quad (3.9)$$

These electric field values are on the order of 10^{-10}-10^{-13} V/cm for typical sample dimensions and current density rates. This is several orders of magnitude below the usual electric field criterion for transport of 10^{-6} V/cm. Not only do these measurements allow us to increase the electric field phase space[25, 26] in which we probe, but the electric fields accessed by SQUID magnetometry are actually more appropriate for many applications.

This lower electric field criterion does pose a significant issue when comparing J_c determined by SQUID magnetometry to data determined by traditional transport measurements, with its usual electric field criterion of 1 μV/cm. One solves this problem by using the well-known phenomenological power law relation[11] $E \propto J^n$. Later we will compare data between transport and SQUID magnetometry and by using this relation, we will see that the data compare very well.

Creep Measurements

If one wants to study the current decay of superconductors, SQUID magnetometry can be used. It has been shown that the decay of the irreversible magnetization is

equivalent to the decay in the critical current density[27]. Over fairly long timescales, the logarithm of the irreversible magnetization decays with the logarithm of the time. As can be seen in figure 11, this decay is linear.

We can then define the creep rate parameter $S = -\frac{dln(J)}{dln(t)}$. This parameter is temperature dependent as can be seen in figure 12. Figure 12 is a typical plot of *S* for a sample with correlated disorder. Creep measurements can give many types of information not only about the electric field criterion of SQUID measurements but they also lend information about the types of disorder in the superconducting matrix. Lastly, by understanding the decay in the irreversibility magnetization, one can obtain the pinning energy of the superconductor by using Maley analysis[28].

Expanding to Angular Methods

A major focus of this thesis is the expansion of traditional contact-free methods to allow for angular study of critical current densities. This would allow one to explore the angular dependence of the critical current density at lower temperatures and electric fields and any available magnetic fields. One can define the angle θ such that it is the angle that the applied field, *H*, makes with respect to a normal to the sample surface. This new tool presents one with several challenges that will be discussed and the solutions that allowed us to expand the above described methods.

The MPMS-7 model we used for these experiments had both a longitudinal and transverse pick-up coil. Figure 13 is a sketch of the sample situated in the two different types of coils. The sample is mounted on a horizontal rotator so that the sample surface can be rotated with respect to *H*. The magnetometer can then determine the longitudinal

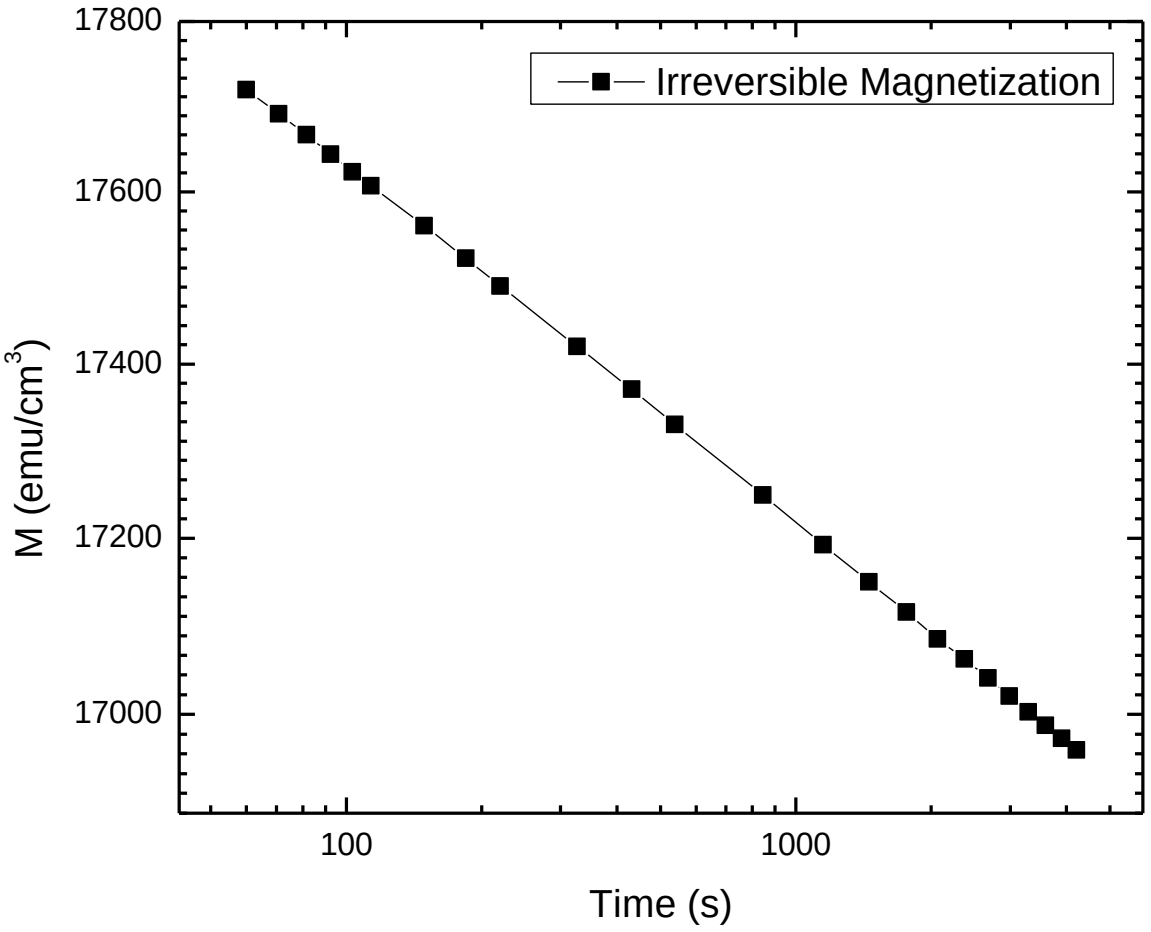

Figure 11: The logarithmic decay of the magnetization as a function of time tends to be linear over long time scales. This quantity is directly related to the decay of J_c.

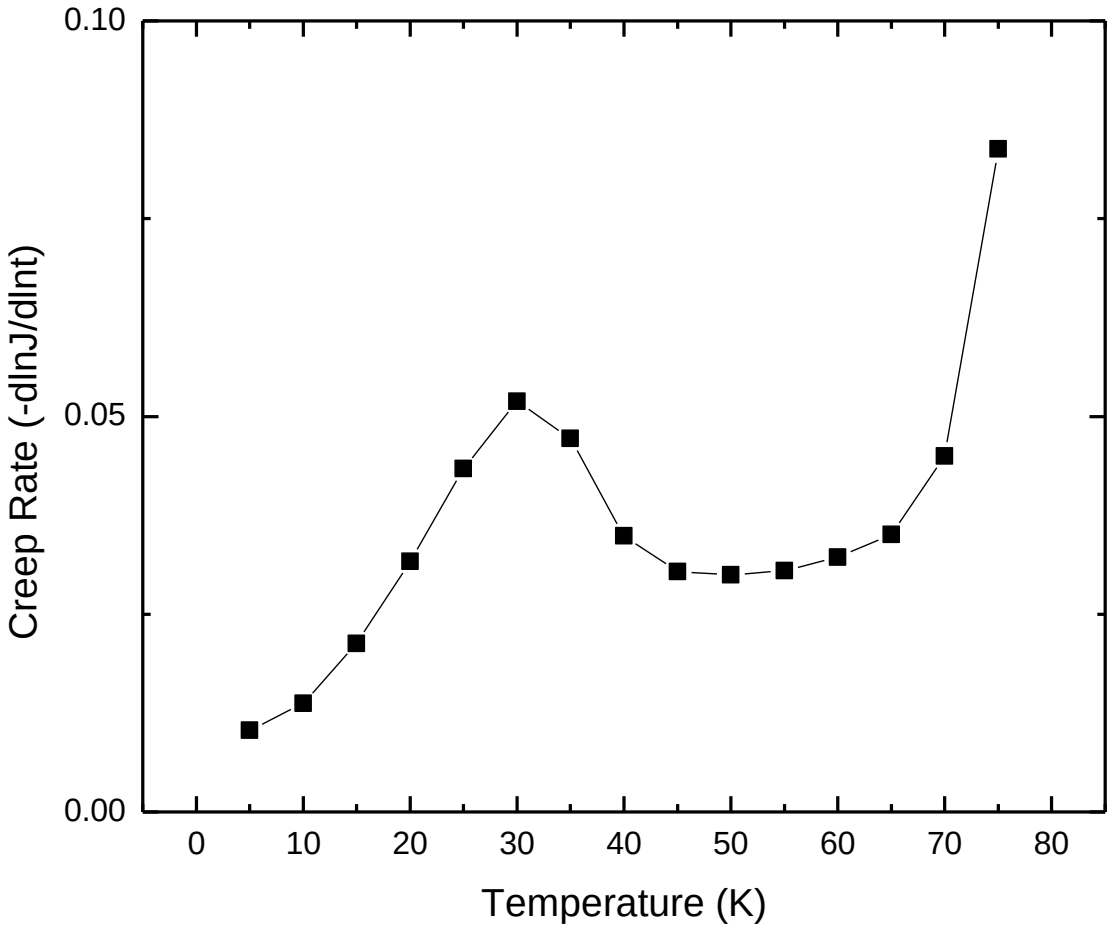

Figure 12: The creep rate *S* can be measured by SQUID methods. This value is temperature dependent and related to the electric field *E* determined by magnetic measurements of current density.

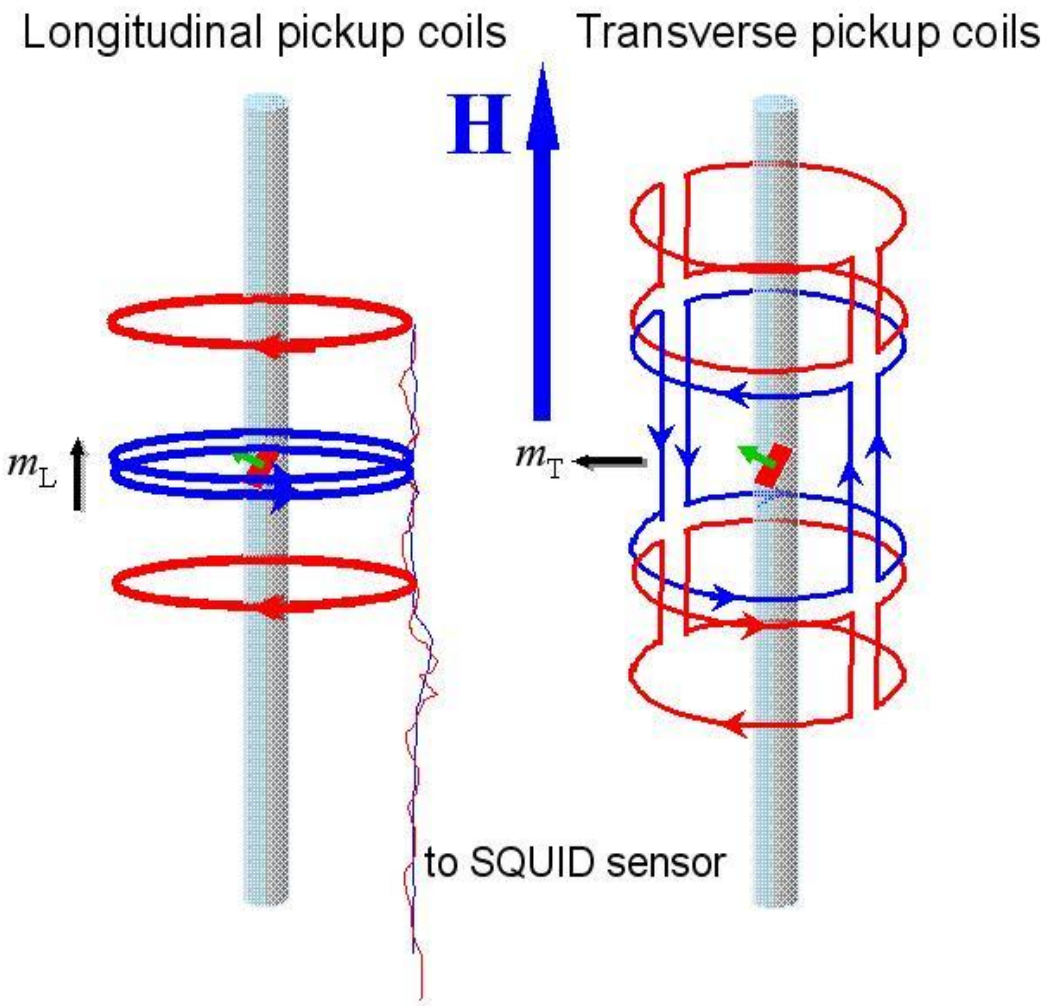

Figure 13: A sketch of a sample in a magnetometer with longitudinal or transverse SQUID pick-up coils. We are able to determine both the transverse and longitudinal moments produced by the J_c in the tilted (or rotated) superconductor.

and transverse magnetic moment. This also allows one a way to determine the angle *in situ* as well. In reality, the two coil sets are wound over one another, so that the same sample positioning and translation allows sequential measurement of the longitudinal and transverse components of the magnetic moment vector.

The next problem addressed was to ensure that there is no cross-talk between the longitudinal and transverse SQUID pick-up coils. This was achieved by changing the centering settings for the transverse SQUID to "linear regression" mode. To ensure that no cross-talk occurred, one could produce a remnant moment and rotate it though 360 degrees. This was done on a representative sample at 50 K and the results are plotted in figure 14. As can be seen in figure 14, the transverse moment and longitudinal moment are offset by 90 degrees and the total moment (produced by taking the Pythagorean sum of the components) is constant.

The Bean model described earlier is specifically for when H is perpendicular to the sample surface. When one rotates away from this configuration, one needs to use a generalized version of the Bean critical state model[29]. Because the currents flowing in the vertical edge of the superconductor will not experience the full Lorentz force, one must consider a critical state model that includes a J_x and a J_y that can be different. For the configuration seen in figure 15 with $b>a>>d$, where a and b are sides of the strip and d is the thickness of the sample, the generalized Bean model describes J_y (where $J_x>J_y$) in equation 3.10.

$$J_y = \frac{40M}{a\left[1-\frac{a}{3b}\left(\frac{J_y}{J_x}\right)\right]} \tag{3.10}$$

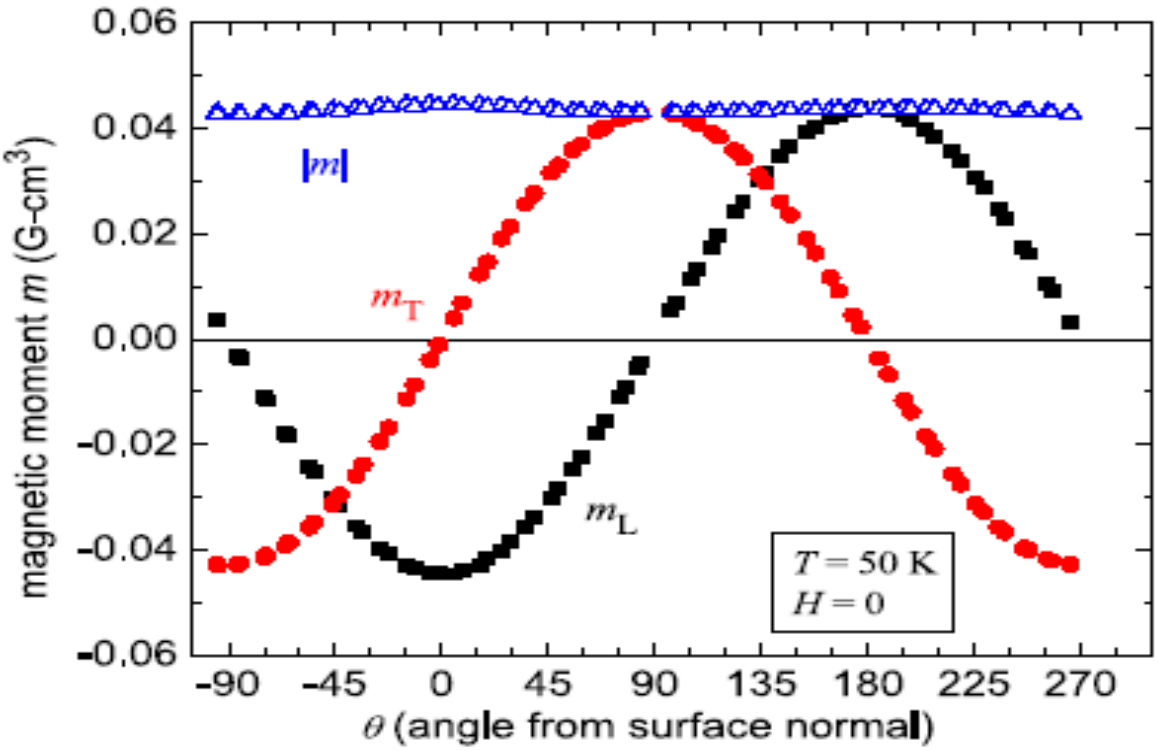

Figure 14: Here we see a remnant moment rotated through 360 degrees. The total magnetic moment is constant over the whole angular range, proving we have minimal cross-talk between the longitudinal and transverse SQUID pick-up coils.

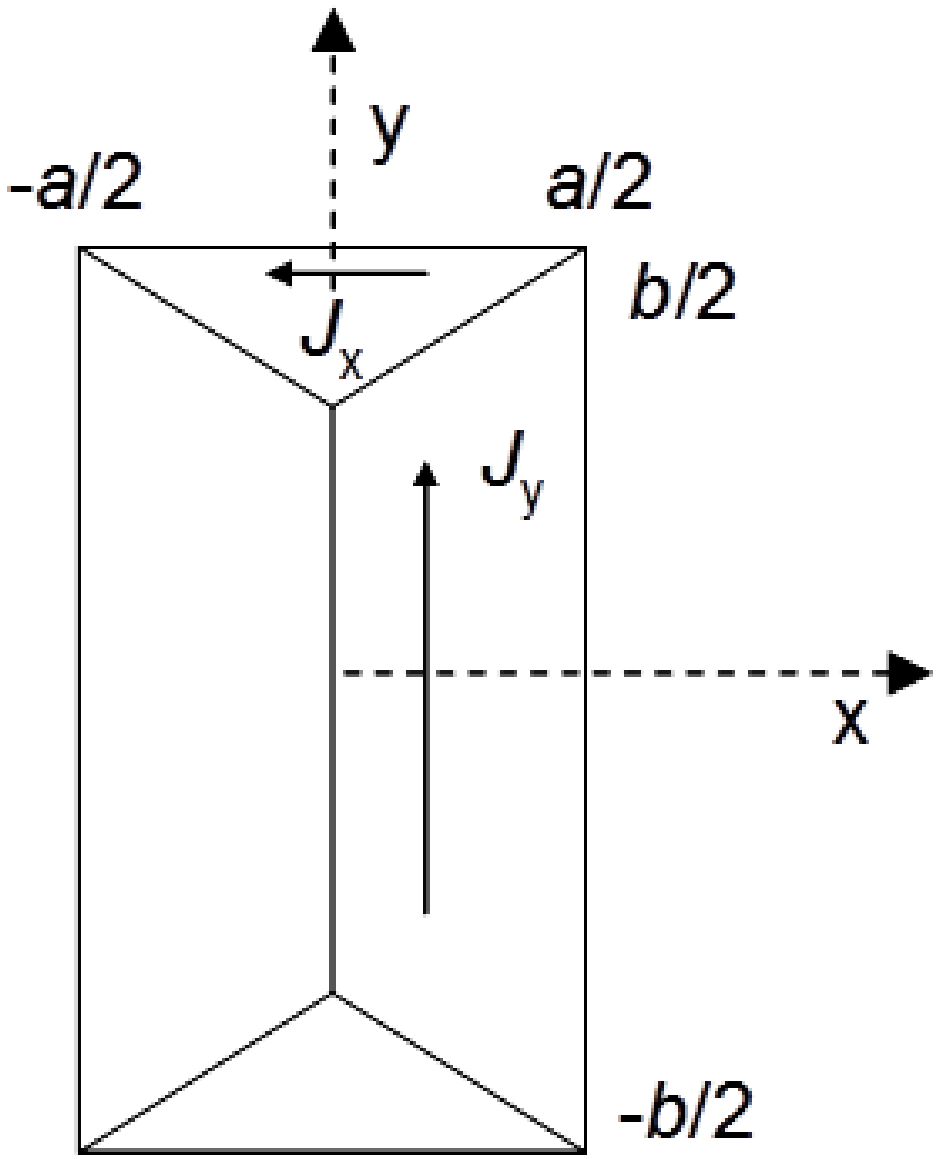

Figure 15: Configuration of superconductor for which the generalized Bean model is developed. Here $a< b$ and $J_y<J_x$.

The term $\frac{J_y}{J_x}$ is an anisotropic term that describes the difference between current densities flowing in the *y* and *x* axis directions. If we then write down the original Bean model assuming that $\Delta M = 2M$, we obtain

$$J_c = \frac{40M}{a\left[1-\frac{a}{3b}\right]} = J_y \frac{\left[1-\frac{a}{3b}\left(\frac{J_y}{J_x}\right)\right]}{\left(1-\frac{a}{3b}\right)} \tag{3.11}$$

One can now compare our calculated J_c to the true J_y value at different ratios of $\frac{a}{b}$. The smaller the ratio of $\frac{a}{b}$, the closer J_c is to the actual J_y. In figure 16 we have plotted $\frac{J_c}{J_y}$ for different $\frac{a}{b}$ values against the anisotropy parameters $\frac{J_y}{J_x}$. To minimize this error, the sample should be patterned into narrow strips. In these experiments, we make the ratio $\frac{a}{b} < \frac{1}{10}$ which translates to a difference between J_y and J_c of less than 4%. We used a laser scribe to striate all of our samples that had angular characterization, as can be seen in figure 17.

By using this new equation, we are able to determine the angular J_c and determined the angular critical current density profiles of different samples over a large phase-space. We first determine the longitudinal and horizontal irreversible magnetic moment measured during hysteresis loops and determine (through Pythagorean sum) the total irreversible magnetic moment at constant temperature and angle. We then use the Bean generalized model to determine the angular J_c for our sample. Lastly we invert the

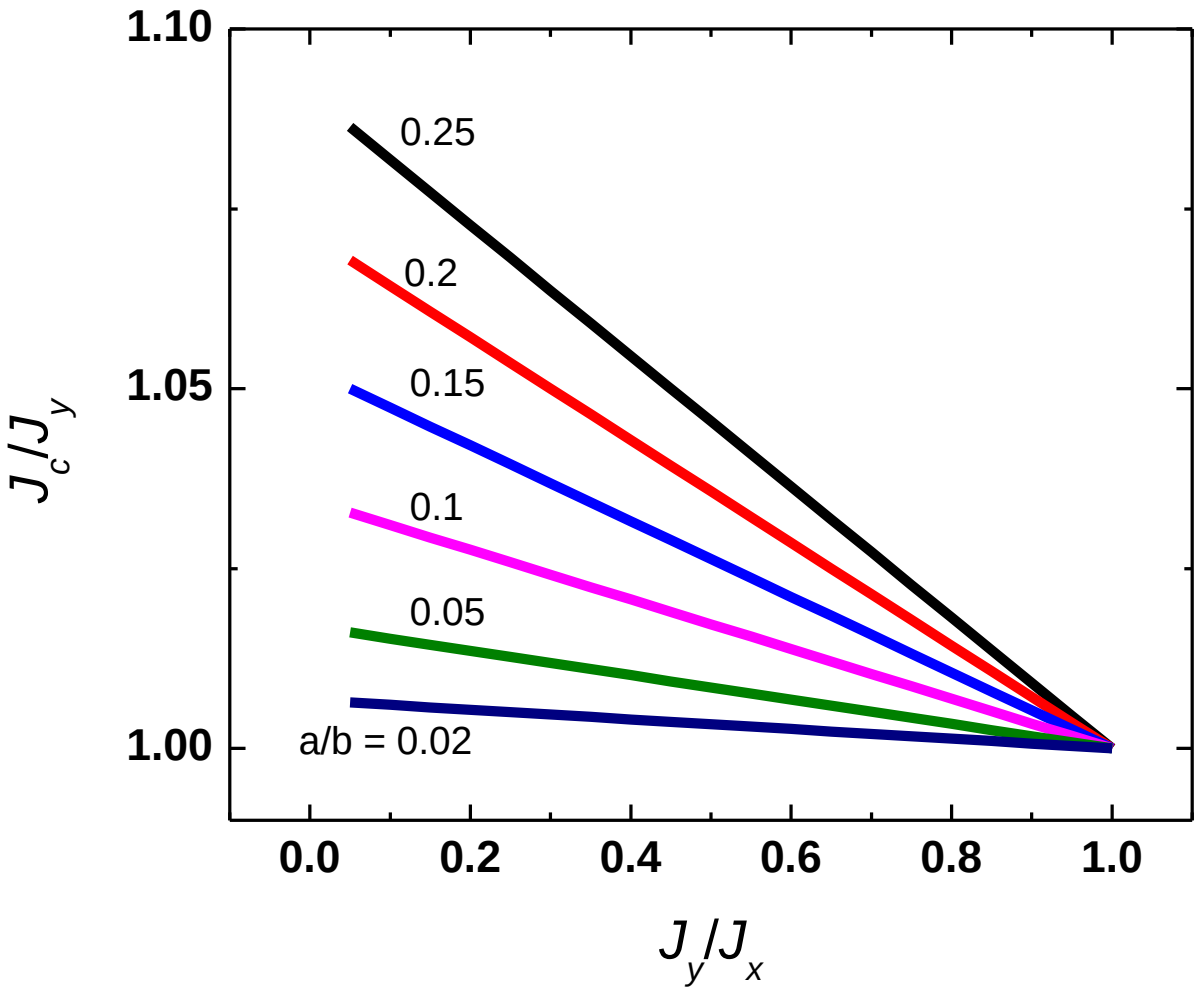

Figure 16: J_c/J_y is plotted with respect to the anisotropy parameter J_y/J_x. Here we see that as long as the sample is patterned into narrow strips, there is not much error due to the rotation of the sample, with "return currents" at the end of the strip that do not experience a full Lorentz force.

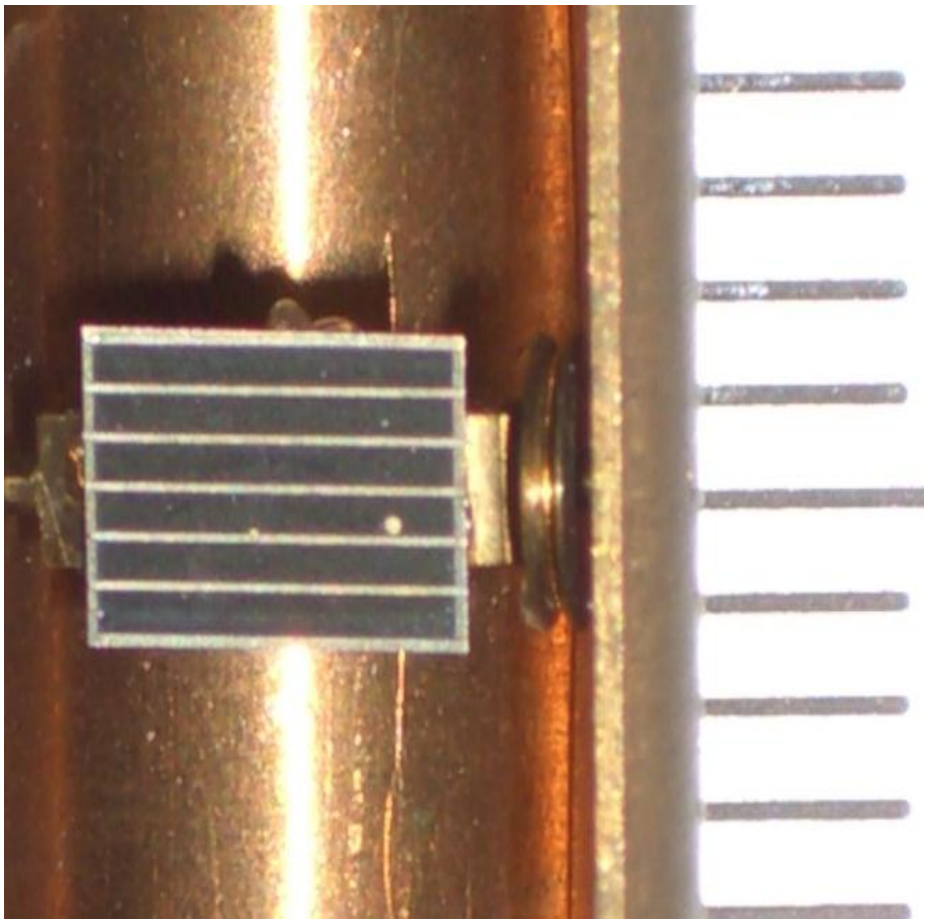

Figure 17: An example of one of our samples. The sample is laser patterned into thin strips and then mounted on a horizontal rotator for measurement in a vertical magnetic field. The scale markers on the right are intervals of 1 mm.

data to determine the dependence of J on magnetic field orientation θat constant applied magnetic field and temperature.

The last consideration is that the sand-pile method would not be valid after a critical angle is exceeded, which occurs when the roof-top changes configuration directions[29]. This angle is approximately $\theta_c \approx \tan^{-1} {}^{a}/_{d}$ which is ~89 degrees. This angular range is excluded anyway, though, because full penetration could not be achieved with our 7 T magnet. Now the development of an angular extension of the traditional SQUID contact-free methods for studying superconductors has been explained.

Lastly, to compare this method to transport methods, we measured a sample from the same superconducing tape, both by transport and SQUID angular methods. We then scaled the J_c values to account for the difference between the electric field criteria. Figure 18 shows the results. Results from the two methods agree well, once scaled.

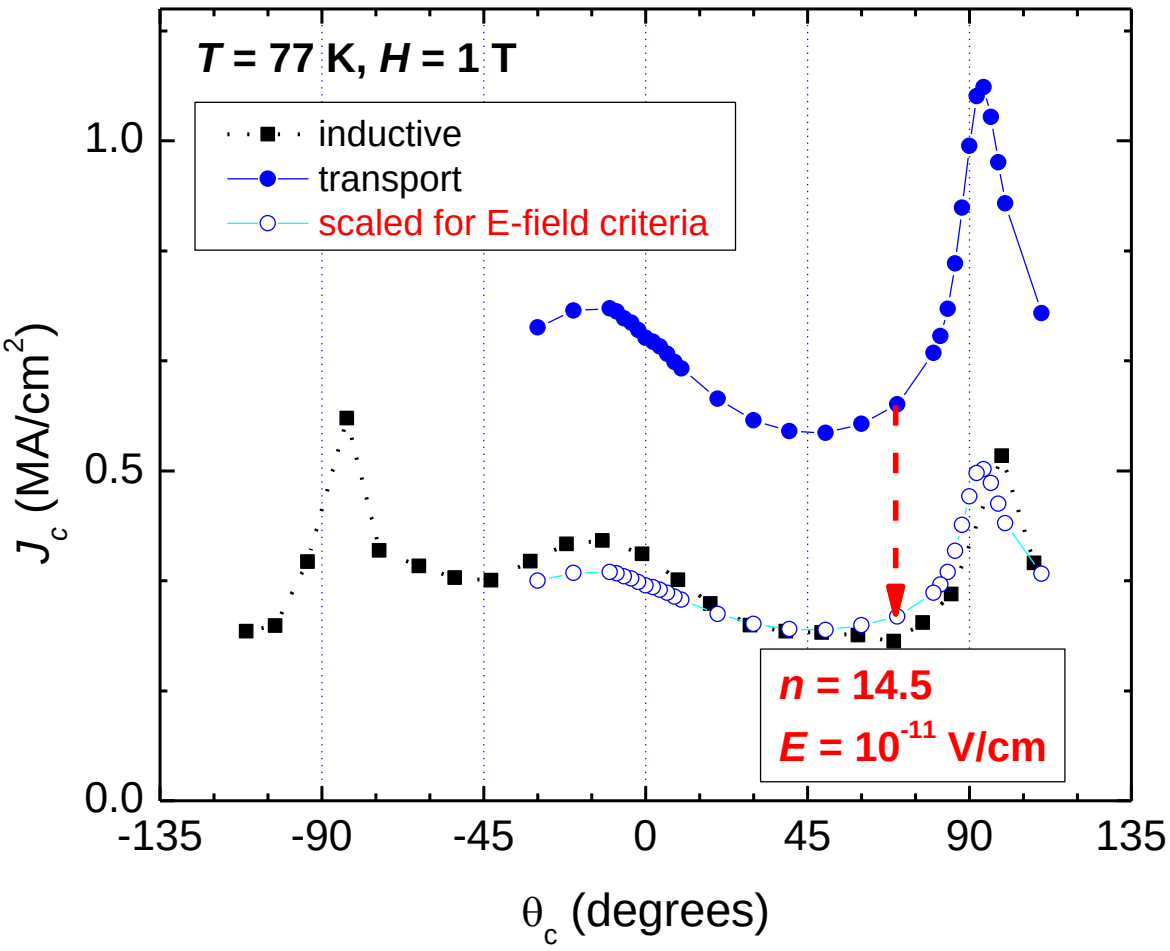

Figure 18: Comparison of traditional transport measurements and SQUID angular measurements. The blue closed symbols are data from transport measurements using an electric field criterion of 1 μV/cm. The blue open symbols are scaled to the lower electric field criterion determined for the contact-free measurements. After the scaling, the two methods agree well.

4 CASE I: DOMINATED BY COLUMNAR DEFECTS

A major goal for developing orientation-dependent, contact-free methods for determining the critical current density of superconducting samples was to study different, distinct and typical pinning landscapes over a large phase-space, including temperatures and electric fields. The first case investigated was a material for which the pinning is dominated by columnar defects. The YBCO sample was produced by pulsed laser deposition on a single crystal $LaAlO_3$ substrate and it contains $BaSnO_3$ (BSO) columnar defects[30 31]. The sample was cut to 0.38 cm by 0.29 cm. The sample was first characterized in a traditional manner, with $H \parallel c$-axis, using SQUID magnetometry to ensure the integrity of the sample before laser scribing it for angular measurements. The sample was then laser scribed into long, parallel 0.4 mm wide strips to allow for measurements of current density versus magnetic field and orientation using SQUID magnetometry, as described earlier. It was also laser scribed around the edge to remove any material that may have been damaged during the cutting of the sample. The sample has a T_c of 88 K.

The BSO columnar defects, as can be seen in figure 19, are self-assembled nanoparticles that align on top of each other. These pseudo extended defects are well aligned with the *c* axis. It will also become important later on that the self-assembly process creates a pin landscape where the columns avoid each other. Each one of these pins can accommodate one vortex even though the column diameter is several times the ξ of this material. Mkrtchya and Schmidt found the saturation number, n_s, of vortices

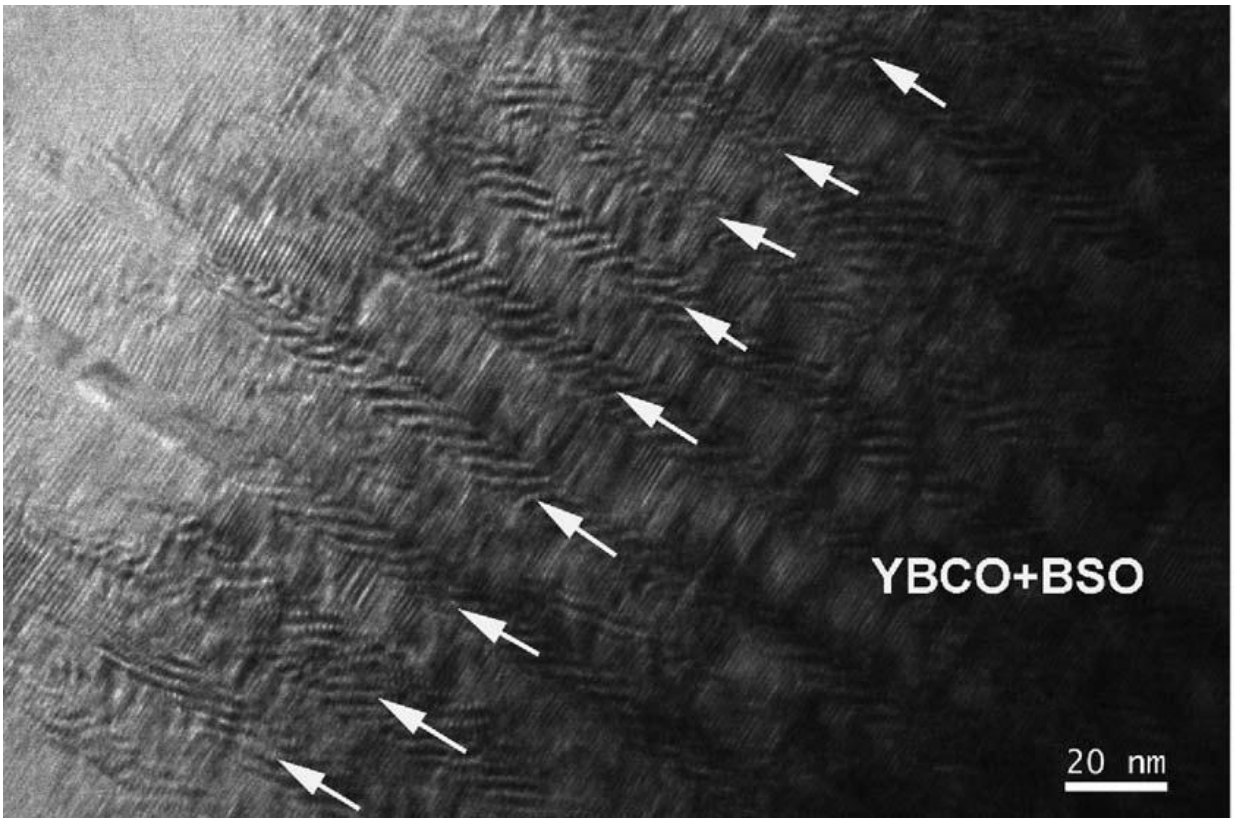

Figure 19: YBCO sample with self-assembled BSO columnar defects. The defects are well aligned to the *c* axis and are self-avoiding.

for a pin of radius *r* as seen in equation 4.1[32]. For this sample, the saturation number is 1.

$$n_s \approx \frac{r}{2\xi_{ab}} \quad (4.1)$$

Temperature Evolution Studied by SQUID Magnetometry

The sample was prepared to have no other engineered defects other than the BSO columnar defects, but there will always be some presence of natural isotropic defects. This situation should create a defect landscape that pins in a very angularly selective way. Also because the pins are very well aligned with the *c* axis, the extra J_c produced due to pinning should fall off very quickly as the sample is rotated from the *c* axis. As can be seen in figure 20, which is exactly what occurs at high temperatures. The value of using SQUID magnetometry, though, is the large temperature range that can be investigated. This is most accentuated in the data at 5 K shown in figure 21. At 5 K, the angular selectivity so evident at high temperatures seems to have been completely washed out.

This most simple case that one can investigate gives a new and interesting picture. Here one sees that there is a competition though the temperature phase-space between stronger angular selective pinning and more isotropic pinning. Point-like isotropic pinning is considered to be weaker pinning, but in fact it becomes more important and dominates over angularly selective pinning at lower temperature, even in in this pinning landscape where the most visible pinning sites are columnar.

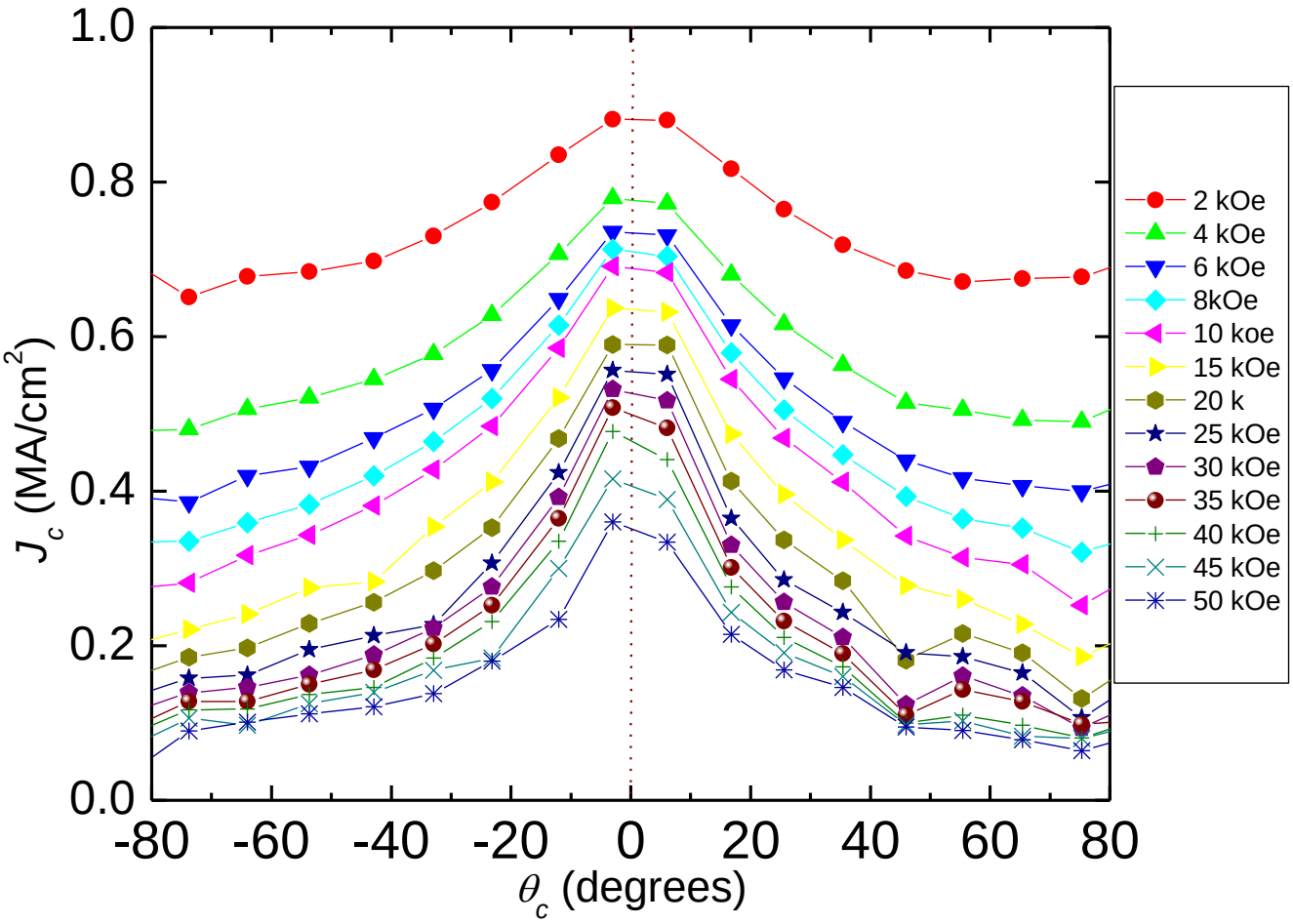

Figure 20: At 65 K the sample shows typical angular selectivity of the pinning landscape. There is a peak in the J_c when the magnetic field is aligned perpendicular to the sample surface, which happens to correlate well with the *c* axis in this sample, which one expects in a sample dominated by columnar pinning defects.

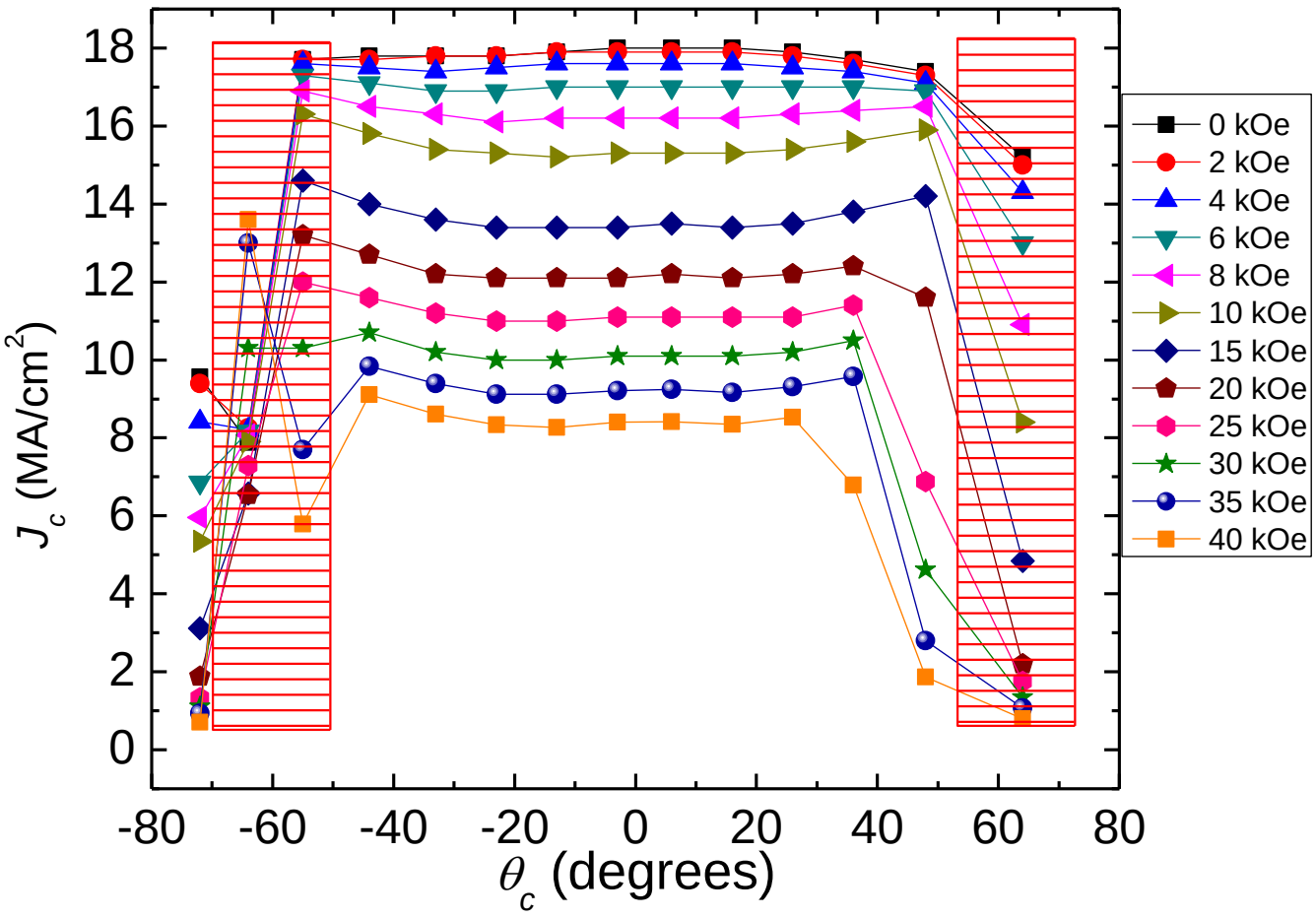

Figure 21: At 5 K the angular selectivity seems to have been washed out of the sample. The intrinsic or up-turn in the J_c does not seem to be present. In the red hatched area, full penetration could not be achieved due to the sample thickness.

One may now be interested in finding other evidence of competition between isotropic pinning and strong columnar pinning. With magnetic measurements, one can now turn to a finer study of the current densities over a large temperature range.

This is one of the important advantages that contact-free methods provide over traditional four point transport measurements. Also measurements of the current density as a function of time can be studied both with traditional magnetic relaxation as well as orientationally dependent magnetic relaxation measurements.

Matching Field Effects

Columnar defects should efficiently pin one vortex per defect. The magnetic flux density that is equal to the columnar pin density, given by equation 4.2, is the "matching field" or B_Φ. In equation 4.2, ϕ_0 is the magnetic flux quantum and *d* is the average spacing of the pins.

$$B_\Phi \sim \phi_0 / d^2 \tag{4.2}$$

In early work by Martinoli and collaborators, an additional contribution to the critical current density in thickness-modulated thin films was observed in magnetic fields having vortex densities commensurate with the modulation[33 34]. As techniques in lithography advanced, it became possible to fabricate regular arrays of pinning sites, with elegant demonstrations of matching effects. For example, Baert et al. showed a periodic local maxima at multiples of $B_\Phi = 10$ G in the irreversible magnetization of niobium films[35]. In continuous superconducting thin films deposited over a regular array of magnetic nickel dots, the electrical resistivity below T_c in a magnetic field was observed to dip at integer multiples of the matching field of 140 G[36]. Similar phenomena have been

observed in the critical current density of high T_c thin films patterned to contain a square array of relatively large holes at a density that results in a 21 G matching field. A series of J_c maxima was observed when there was an integer or rational ratio of pin spacing to vortex spacing[37]. Matching field effects have also been seen in iron arsenide 122 materials with self-assembled nanopillars by Zhang et al. with a much larger matching field of ~8.5 T[38]. Given these results one may assume there should be a distinct feature in the J_c of the material dominated by BSO columns when the applied magnetic field is equal to the matching field.

Using traditional magnetic measurements to determine the critical current density of this sample with the magnetic field perpendicular to the sample surface, one may survey the J_c over a large temperature range. As can be seen in figure 22, there is a sharp decrease in the current density at ~3.5 T over a large temperature range (above 30 K). This kind of phenomenon is indicative of a geometric matching effect, which one could correlate to a matching field effect. It is also interesting to note that the sharp feature disappears at still lower temperatures. This is consistent with the lack of angular selectivity in the current density profile studied above.

To determine if this distinct current density feature is related to a matching phenomenon, one should determine the columnar defect density of this sample in an independent manner. This can be accomplished by using scanning electron microscopy (SEM). If a light etching solution is used to remove a thin layer of the surface, SEM should then be able to image the BSO columnar defects. A solution of 0.2% bromine in ethanol was used to etch the surface immediately before placing the sample in the microscope. Figure 23 is a typical SEM image of a companion sample. The average

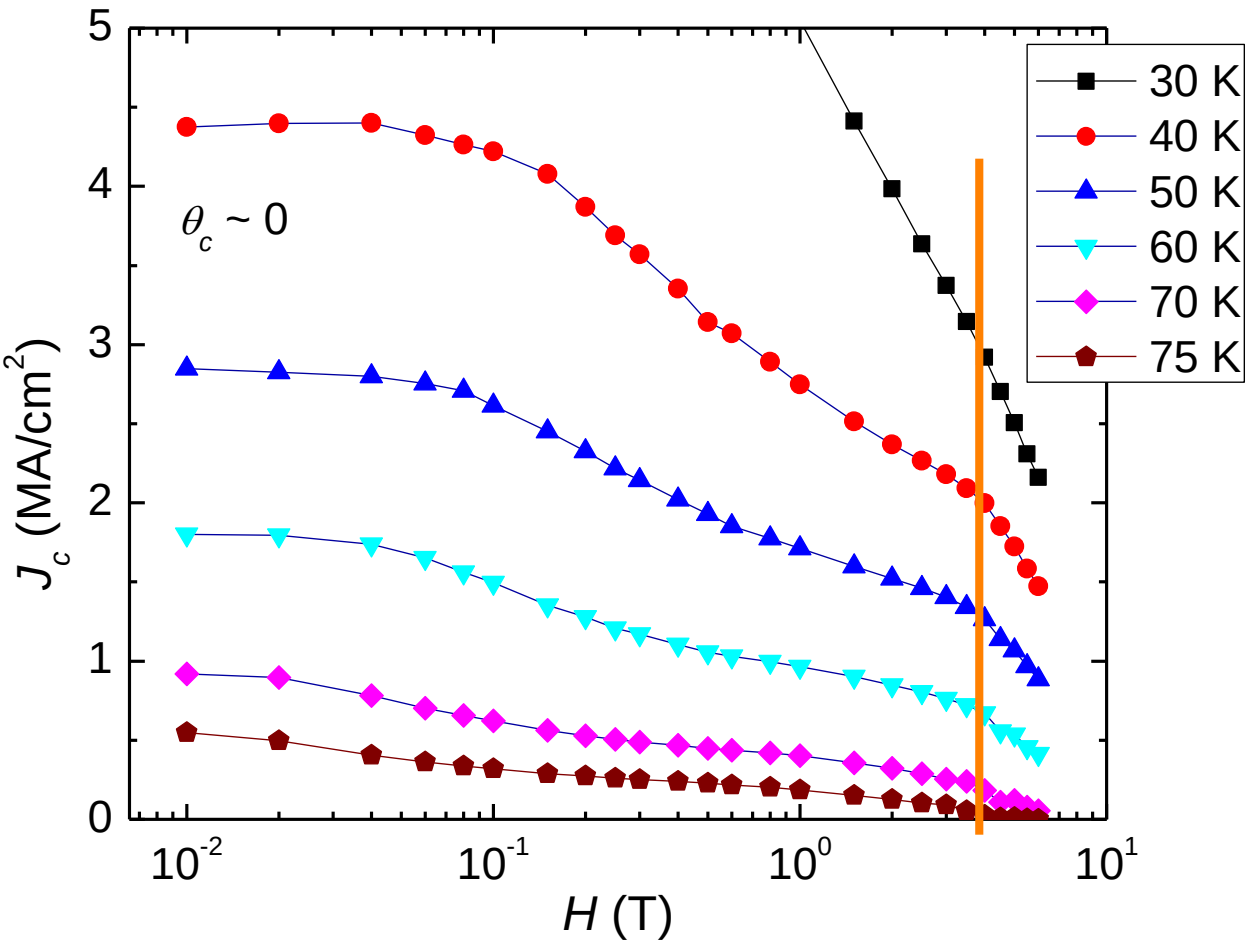

Figure 22: This figure shows the current density profile as a function of magnetic field with a magnetic field perpendicular to the sample surface. There is a drastic falloff in the current density at the same magnetic field over a large temperature range, which is indicative of a matching field effect.

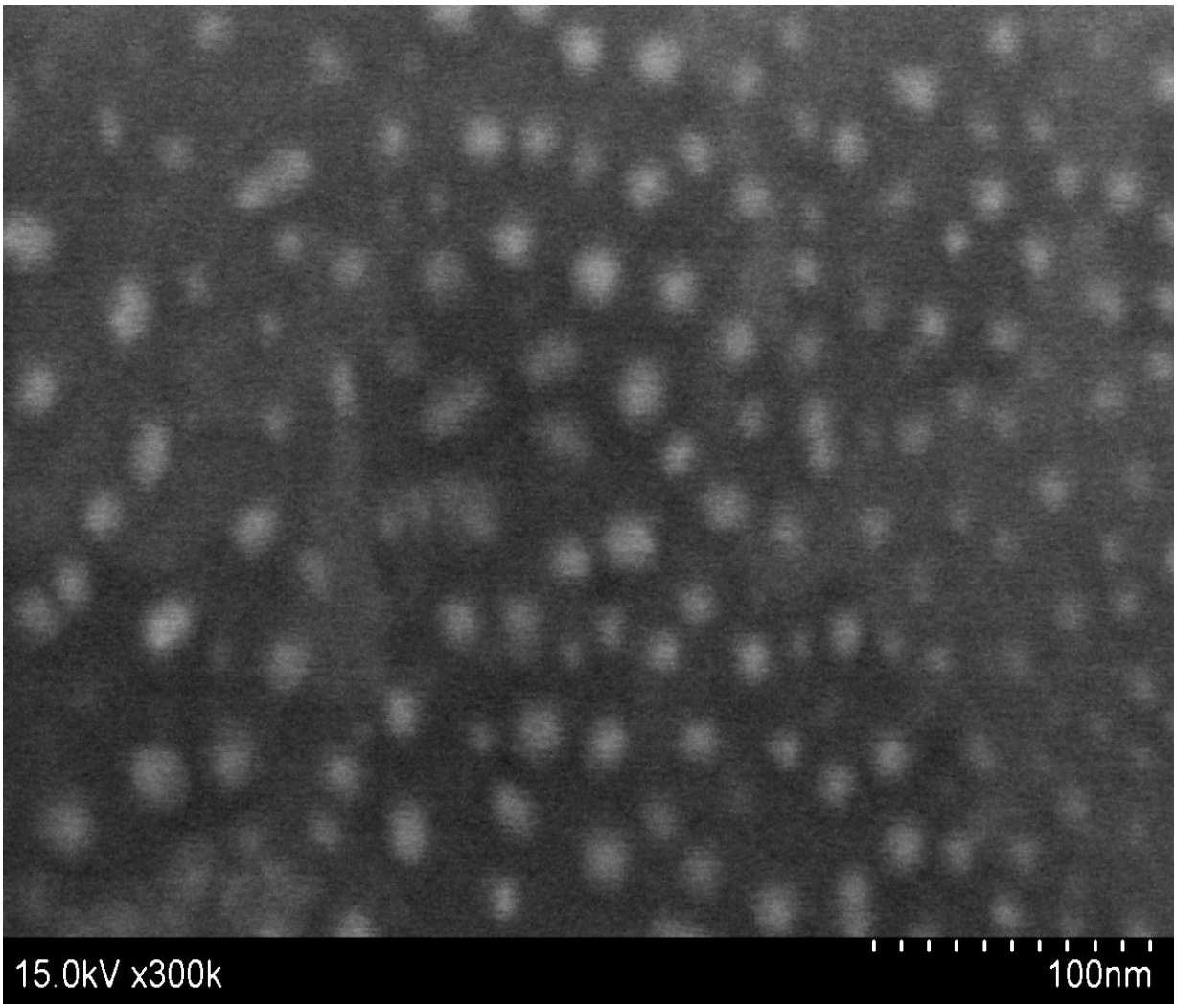

Figure 23: A typical SEM image of a companion sample. The light colored regions are BSO columnar defects. The average defect spacing is ~28 nm. This corresponds to a matching field effect of ~2.5 T ± 0.6 T.

spacing of the columnar defects was ~28 nm. Using equation 4.2, one can then determine the approximate matching field. Equation 4.2 yields a $B_\Phi \approx 2.6 \pm 0.6$ T. This is comparable with the "knee" observed in the current density, though it occurs at a slightly higher magnetic field.

The next question one has is why this sample has such a sharp feature at this magnetic field and why was it not seen in high temperature superconductor materials that were bombarded with heavy ion irradiation. It is likely that the difference originates in the more orderly defect array in the present material. If one looks at the distribution of the spacing between columns in this sample and compare it to that of a random distribution (that is appropriate for heavy ion irradiated samples), there is a distinct difference. Looking at figure 24, one sees that there are no near neighbors in the 0-10 nm box for the BSO sample, while there are many near neighbors in the 0-10 nm box for the random distribution. This lack of near neighbors in the first box should minimize vortex-vortex interactions that would tend to smear out any sharp feature in the current density in the BSO self-assembled samples. One may also note that the sample that Zhang et al. studied had self-assembled nanofeatures and they also observed a similar sharp "knee" feature in the current density at 4.2 K at a high matching field[38].

Another feature that can be studied is the α values over this same temperature range. It is widely observed that the current density of a superconductor follows a power law dependence $J_c \sim B^{-\alpha}$ over a range of intermediate magnitude magnetic fields. According to Blatter et al., a sample with strong columnar defects has an α value of 0 in the single pinning regime[11]. This is not achieved in this material, but abnormally small α values are observed, as can be seen in figure 25. Other predicted α dependences

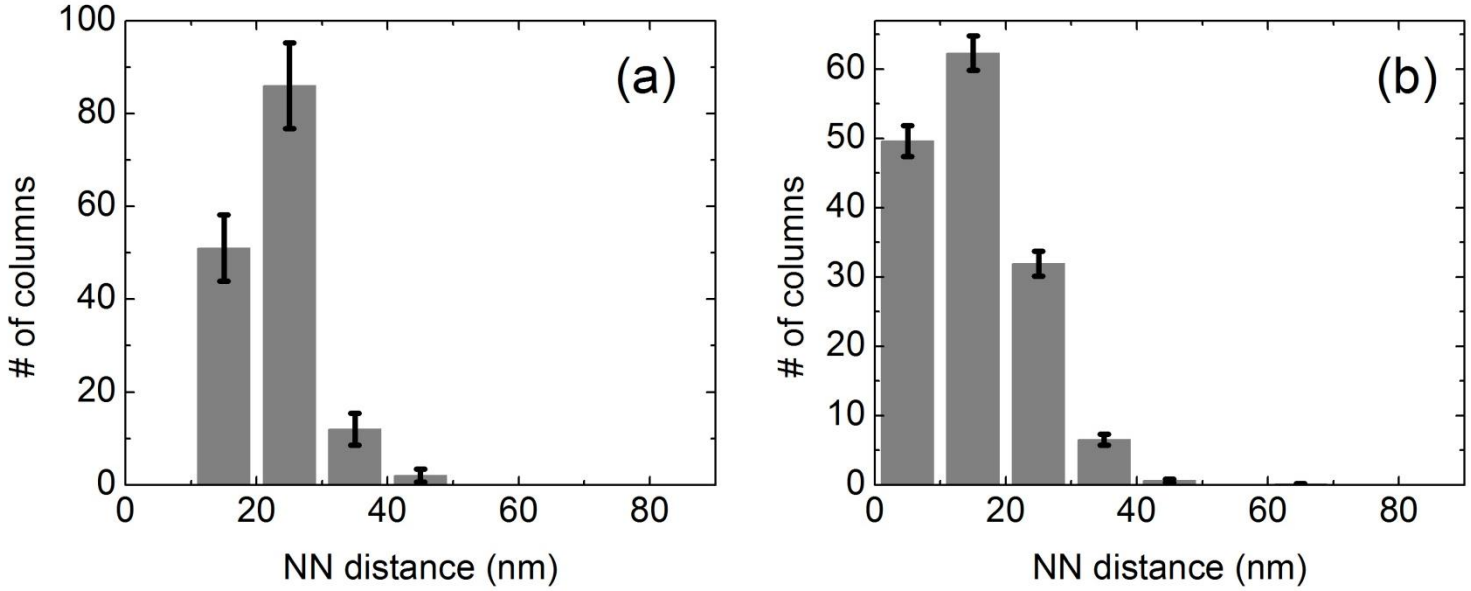

Figure 24: A histogram describing the occurrence of nearest neighbor distances in the columnar defect dominated sample and a random distribution. The sample lacks defects in the first bin which minimizes the energy cost arising from interactions between closely spaced vortices.

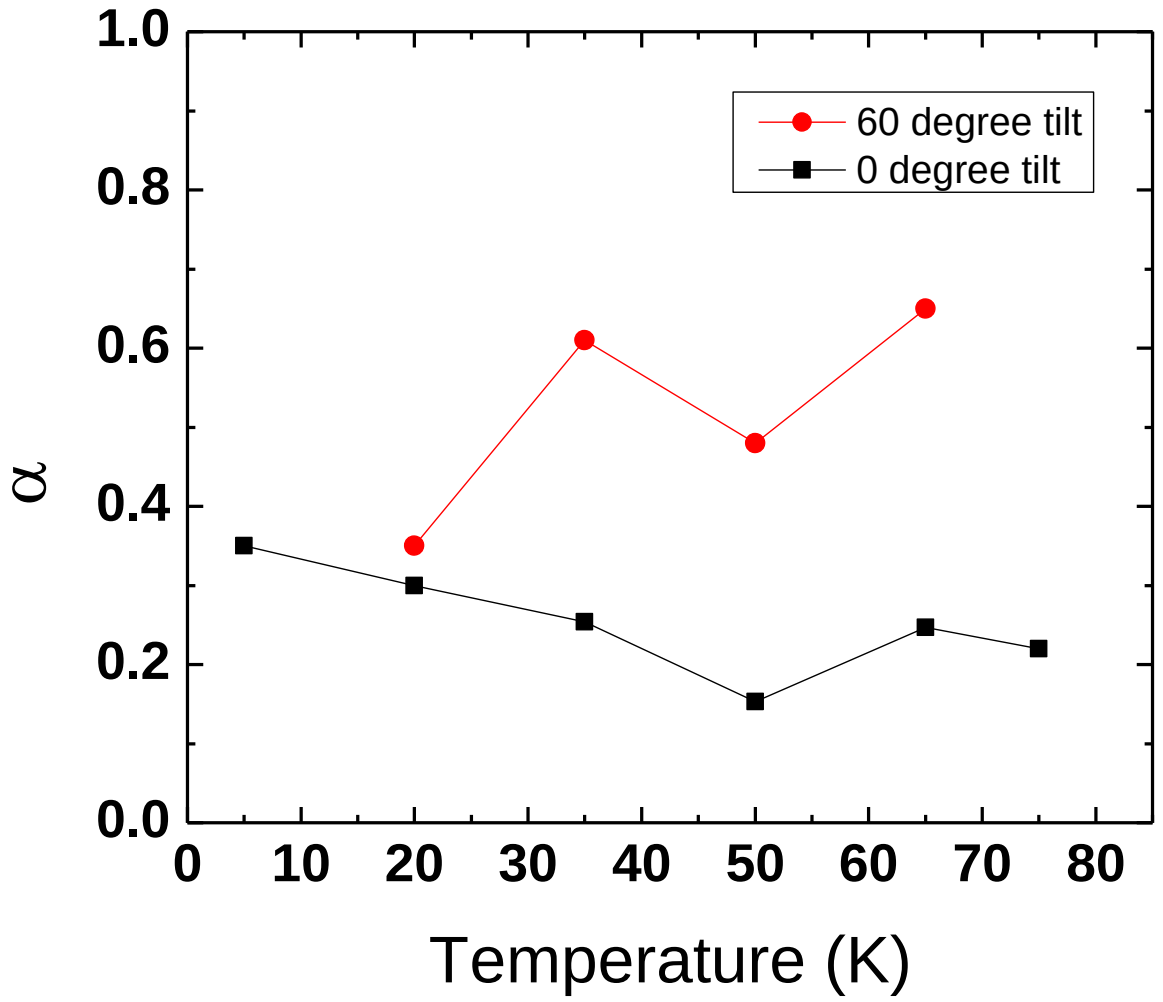

Figure 25: When the magnetic field is perpendicular to the sample surface, it has very suppressed α values at high temperatures. As the sample is rotated away, the α values increase to more typical values at high temperatures.

were developed by van der Beek et al. and Vinokur et al. which predicted α values of 5/8 and 1/2, respectively, for samples with weak collective pinning[39 40]. The α value of 5/8 was predicted for large sparse defects and 1/2 is predicted for point-like defects. Also, Nelson et al. and Blatter et al. predicted α values of 1/2 for plastic pinning and 1 for collective pinning by columnar defects[11 41]. This material has a high temperature α value below 0.3 when the magnetic field is perpendicular to the sample surface, but at lower temperatures the value increases; this is the same temperature region where the angularly selective pinning becomes washed out. These values of ~0.2 – 0.25 seem to paint a picture of a pinning that is not quite truly one vortex per pin pinning. Qualitatively, a likely scenario for this low-α regime in this material is a progressive filling of the columnar defect array accompanied by some falloff in J_c due to a combination of increasing Lorentz force density, competition with increasing inter-vortex forces, and thermal activation. Once the columnar array is filled, the J_c drops abruptly. In further experiments, the sample was then rotated to misorient the columns with respect to the magnetic field, in order to minimize the effect of the columnar pins. In this configuration, the α values at high temperature are much larger, near 0.5 – 0.6, and then the α value appears to decrease to a value similar to that for the parallel configuration at lower temperatures. This again seems to indicate that the columnar defects are not so dominant at lower temperatures.

It is also possible that matching field effects give some explanation to the very low α values observed at high temperatures in samples with columnar defects. When the defect array is underfilled with vortices in fields below B_Φ, every vortex can be pinned. Matching field effects create extra pinning at high fields producing "extra J_c" and lower

the α value. This phenomenon has important technological implications for superconducting thin films in industrial applications.

Conclusions

Using contact-free methods to determine the current-conducting properties of a sample dominated by columnar defects has increased the phase space that can be studied. A consistent picture is produced that shows the importance of angularly selective, strong columnar pinning at high temperatures. At lower temperatures, the angular selectivity seems to be washed out as more isotropic defects increasingly contribute to the overall pinning. Also matching field effects were also seen with B_Φ values near 3 T and confirmed by SEM. This effect is reflected in the α values as well as the raw J_c data. The matching field effects also seem to be washed out at lower temperatures, which is consistent with the loss of angular selectivity in the current density data.

5 CASE II: DOMINATED BY ISOTROPIC DEFECTS

Another typical pinning landscape studied was one dominated by large sparse pinning sites. In the cross-sectional TEM micrograph in figure 26, the lighter parts are second-phase rare earth oxides forming mostly isotropic pinning sites. The precipitates are $(Y\text{-}Gd)_2O_3$ particles that are roughly 8 nm in diameter. These precipitates tend to form into layers near the *ab*-planes. There are also dark long regions that are most likely threading dislocations and antiphase boundaries that may produce some angular selectively. The sample has a T_c of 90.7 K. Again, the sample was cut into a rectangular shape and patterned into long strips for angular magnetic measurements[42]. The experimental results will be compared to the a model proposed by Plain et al. to attempt to understand this different distinct pinning landscape.

Angular Current Density Analysis

This characteristic pinning landscape should have mostly isotropic pinning on top of the intrinsic pinning associated with the layered nature of the high temperature cuprate superconductors. There may also be some small angularly selective pinning producing at most a small peak in the current density at the *c*-axis. Qualitatively, this should result in a J_c minimum at or near the *c*-axis.

Figure 27 shows angular J_c data from this sample at 65 K. The sample seems to have the current density profile that is expected. There is some broad and small peak near the *c*-axis and the current density grows quickly as the *ab*-axis is approached.

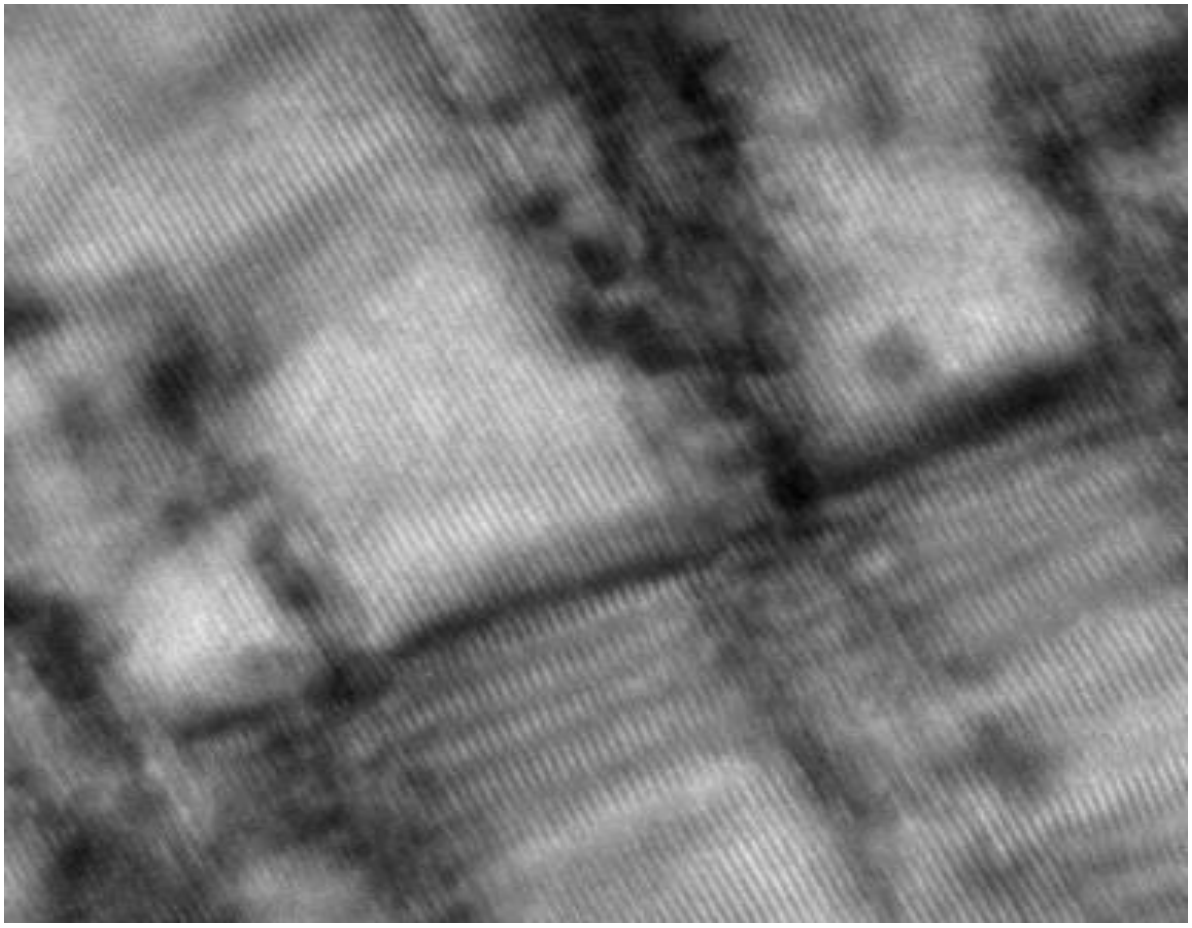

Figure 26: The light sections are second-phase precipitates that are large and isotropic. Also seen are threading dislocations that should produce some angularly selective pinning.

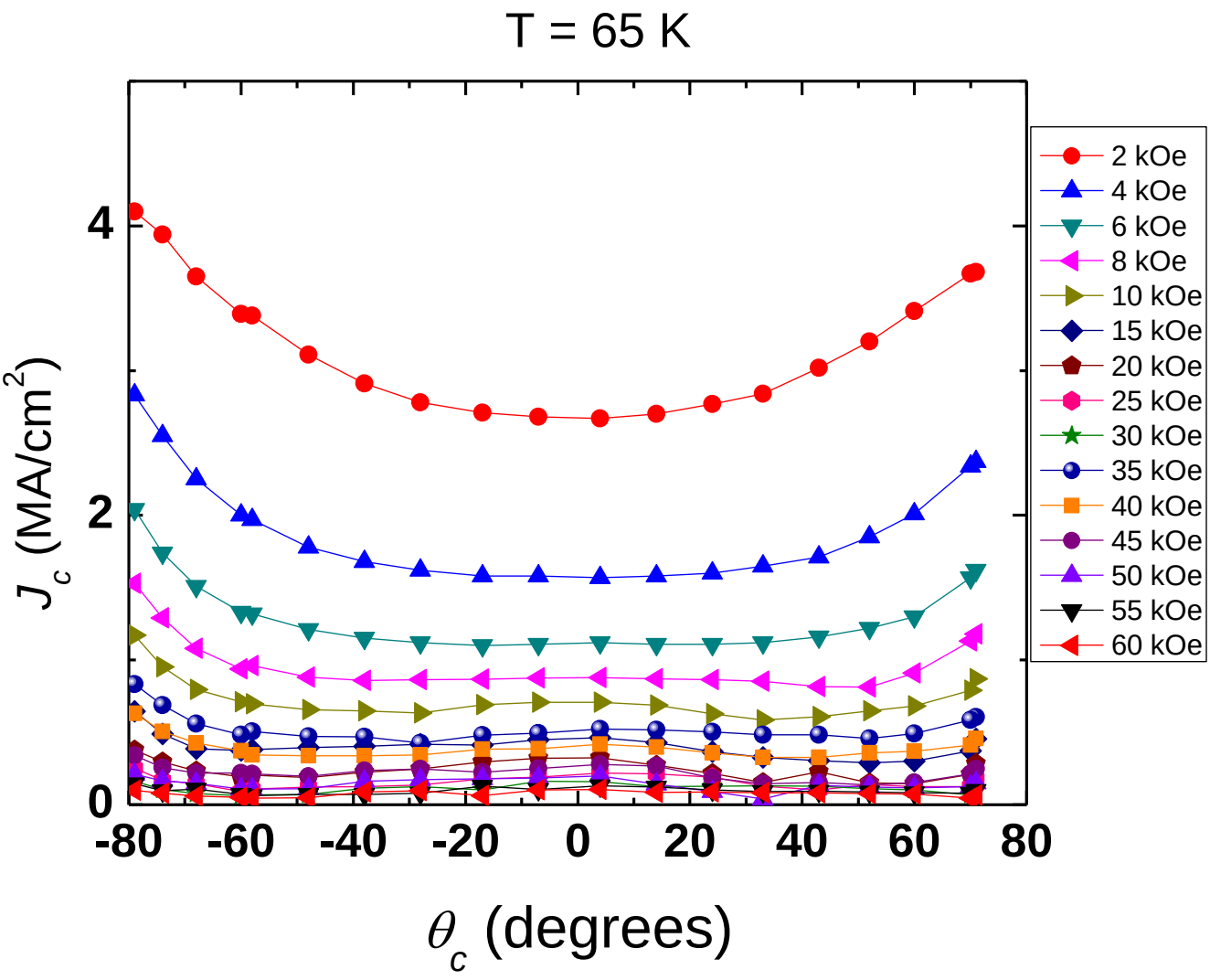

Figure 27: Angular current density profile of a sample dominated by isotropic pins at high temperature (65 K). There is some angular pinning that is probably due to threading dislocations. It is most apparent at high temperatures and large magnetic fields.

The feature near the *c*-axis becomes more pronounced when large magnetic fields are applied to the sample.

Next the sample was cooled to 5 K and angular J_c data were taken again. Once again, as is evident in figure 28, there is little if any angular selectivity in the current density profile. Whatever selectivity is present appears at the highest magnetic fields. This angular profile again show that the pinning landscape is dominated by isotropic pinning because there is a minimum in the J_c near *c*-axis and a maxima as the *ab*-plane is approached. This is expected due to the mass anisotropy, together with the layered defects that tend to align with the *ab*-plane and the intrinsic anisotropy of the layered cuprate materials.

These two figures give a consistent picture of a pinning landscape which has very little angular selectivity. The current density profiles show a large maxima as the *ab*-plane is approached at these representative temperatures and well as other intermediate temperatures.

Looking for Competition

Given that this sample is dominated by isotropic pinning centers, it would be interesting to determine further the relative contributions of and competition between strong and weak pinning. In doing so, we remain mindful that there does seem to be some angular selectivity at high temperatures and large magnetic fields. Using a model that was proposed by Plain et al. one can try to separate the strong pinning of large defects from the weak pinning of point-like defects[20 25]. Plain proposed an equation to fit temperature dependent data for $J_c(T)$ as described in chapter 2. Figure 29 shows the results from

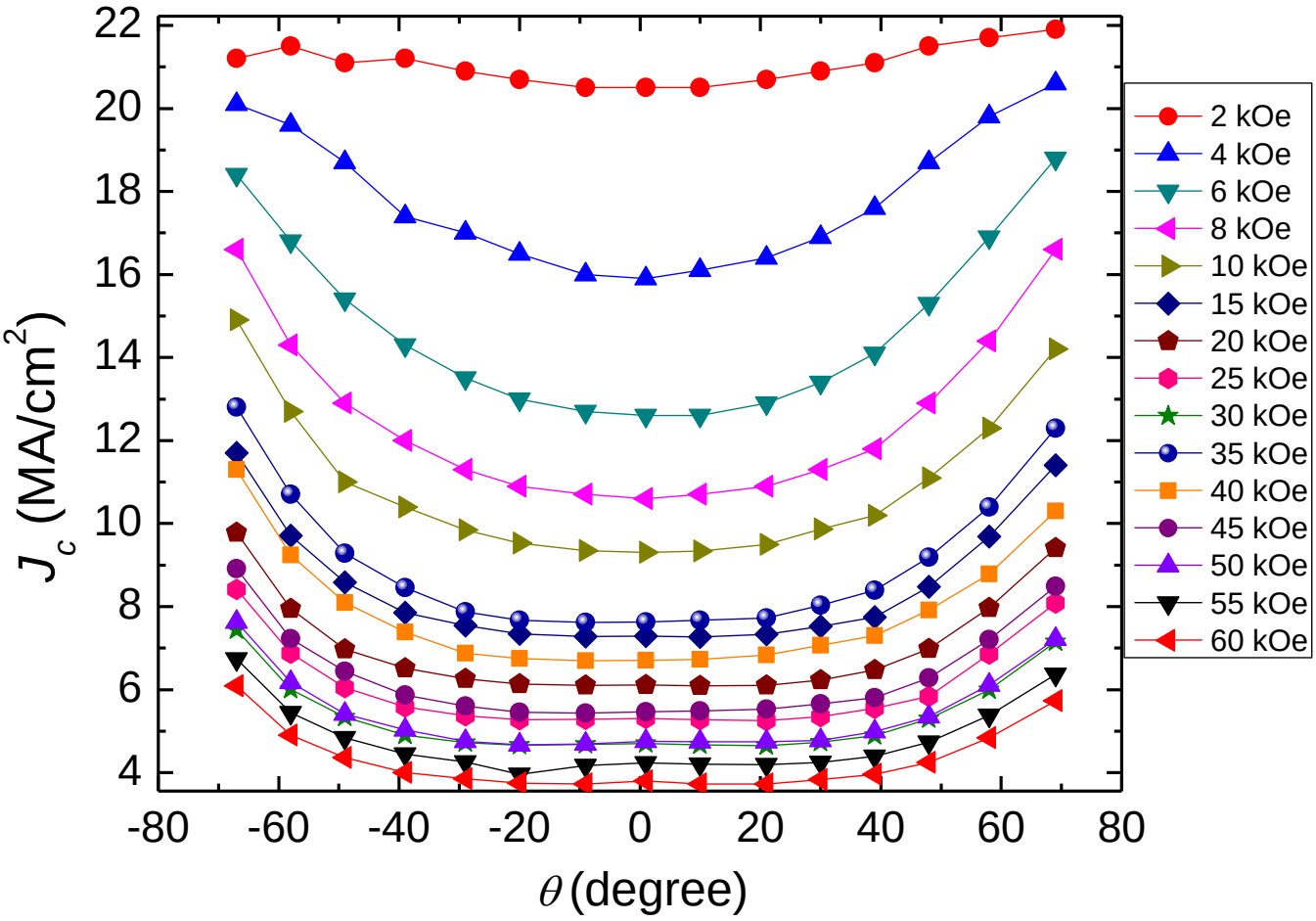

Figure 28: Angular current density profile of a sample dominated by isotropic pins at low temperature (5 K). The angular selectivity seems to once again be washed out.

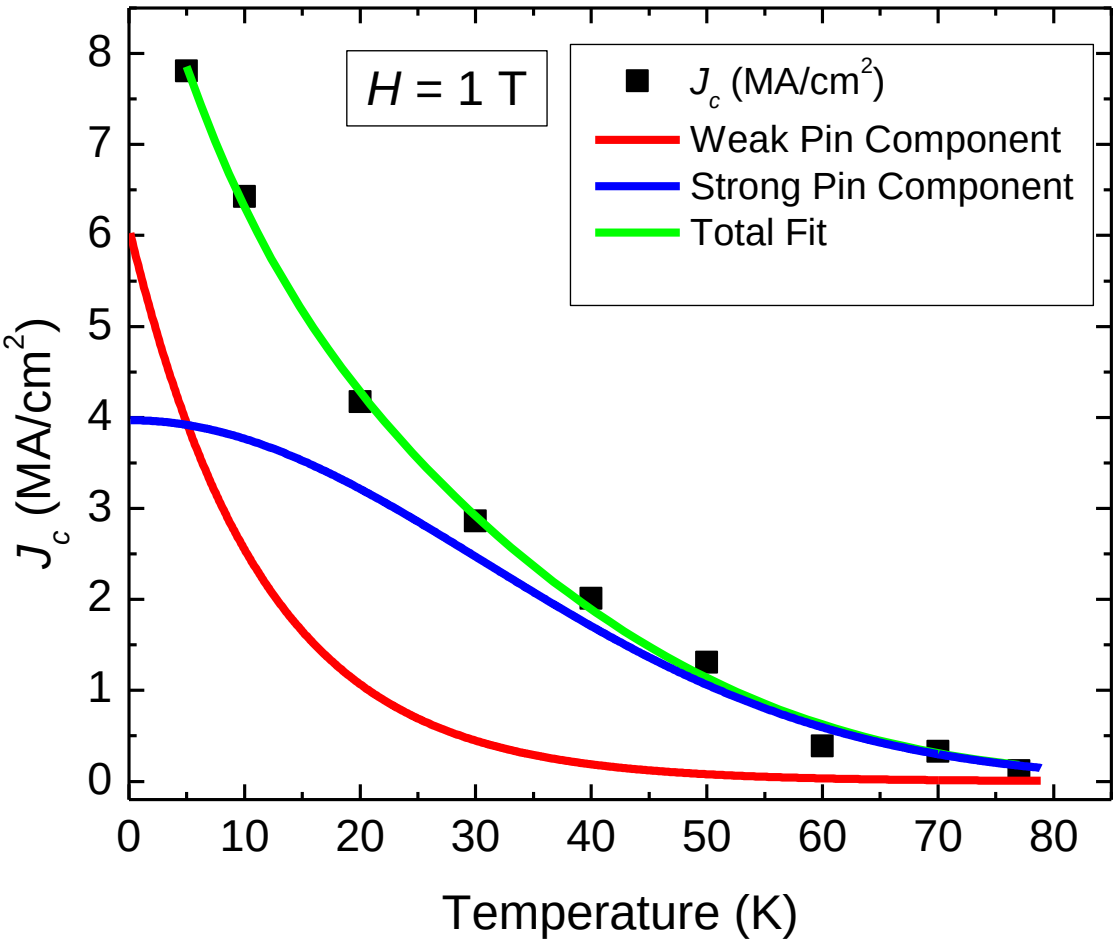

Figure 29: Experimental data fit to the model proposed by Plain et al. The sample seems to be dominated by a strong pinning component.

fitting temperature dependent data for the present material to the model relation of Plain et al.

From figure 29 it is immediately clear that this sample is dominated by strong type pinning. This implies that the large sparse defects dominate the pinning landscape of this sample as opposed to weaker point-like defects. There is also some strong pinning from threading dislocations as described in the first portion of this chapter, but in the current density profile there does not seem to be much angular selectivity even at high temperatures, insinuating that it is a small contribution.

To continue to compare this sample with the sample in case I that is dominated by columnar defects, one may look at the α values in the present case with predominantly isotropic defects. Figure 30 shows the α values of this sample. It does not have the same uncommonly low α values at high temperatures. In fact, the α values are much more comparable to the α values of the columnar sample after it has been rotated by 60 degrees. This is because there are not any significant columnar defects. The lower temperature data seems to collapse to similar values to that of the columnar defects. The values lie largely in the range of 5/8 – 1/2 as predicted theoretically for pinning by large, sparse defects (strong pinning) or point-like defects (weak pinning), respectively. Indeed, the downward trend in α-values with decreasing temperature tracks qualitatively the increasing proportion of the weak pinning contribution evident in figure 29. The material does not exhibit the unusually low α values observed with columnar defects at high temperatures, with the field oriented along the defects. In fact, when the sample from case I was rotated 60° away from the *c*-axis the

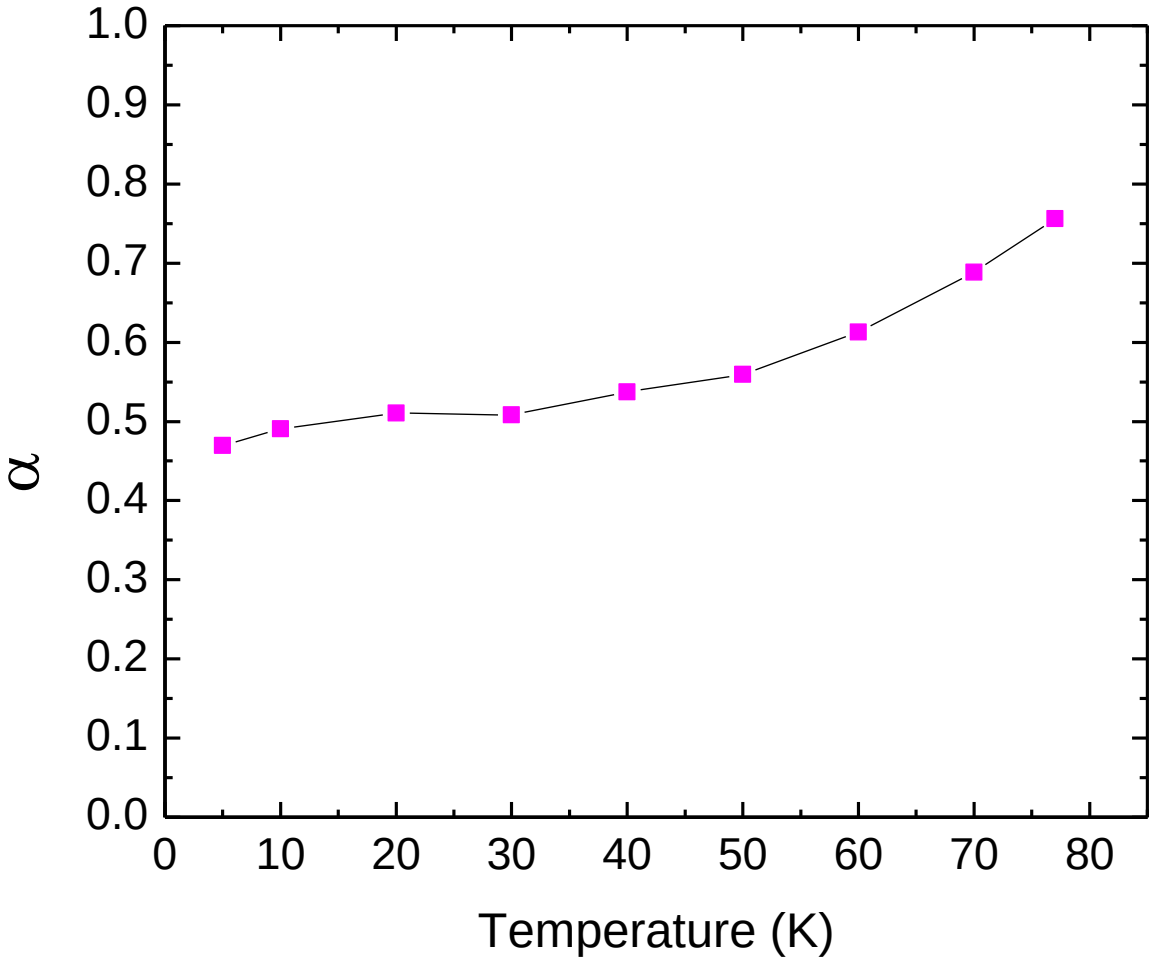

Figure 30: The α values of a sample dominated by isotropic defects. As compared to the sample dominated by columnar defects, the α values do not have very low values at high temperatures.

α values measured are much more comparable to those observed in the present material, case II. At the lower temperatures, the α's for both samples I and II seems to assume similar values near 1/2, characteristic of (individually) weak, isotropic pins.

Conclusions

In this second case dominated by large isotropic defects, it is clear from the Plain analysis that there is a temperature evolution between the relative importance of large isotropic pins versus point-like weak pinning. Even though this sample is dominated by strong pinning similar to the sample studied in case I, it is fundamentally different because of the lack of dramatic angular selectivity in the critical current density profiles. As is evident from figure 30, the α values of this sample fall well within the theoretically predicted values for isotropic pins, as opposed to case I. There are no matching field effects present in the sample, as it has little to no correlated columnar disorder.

6 CASE III: COLUMNAR DEFECTS AND ISOTROPIC DEFECTS

Recently, coated conductors have been synthesized to contain a mixture of both columnar defects and isotropic defects. A sample was studied that contained $BaZrO_3$ (BZO) columnar defects as well as Y-Gd oxide second-phase precipitates, to create a mixture of different types of disorder. These BZO columnar defects are not as well aligned with the *c*-axis as the BSO columns in the sample dominated by columnar defects, case I. This is not bad technologically, because the average ~6° tilt and especially the splay (angular spread in column directions) has some advantages over a very well aligned columnar defect, by forcing some entanglement of vortices and inhibiting their movement[43]. These structural features can be seen in the TEM micrograph presented in figure 31. These types of materials represent some of the most advanced second generation coated conductors developed for demanding applications[15]. This sample was cut into a rectangle and striated into thin strips for angular magnetic measurements[42].

The goal of studying this type of pinning landscape is to understand the competition (and cooperation) between the correlated or strong disorder and the isotropic disorder. This is achieved by studying the angular current density though a large temperature space, as well as modeling the temperature dependence at various constant magnetic fields. These different methods allow different cuts of phase-space to be studied.

Angular Current Density Measurements

As one can imagine, this pinning landscape is much more complicated than the previous two studied. One may anticipate that the current density profile at high

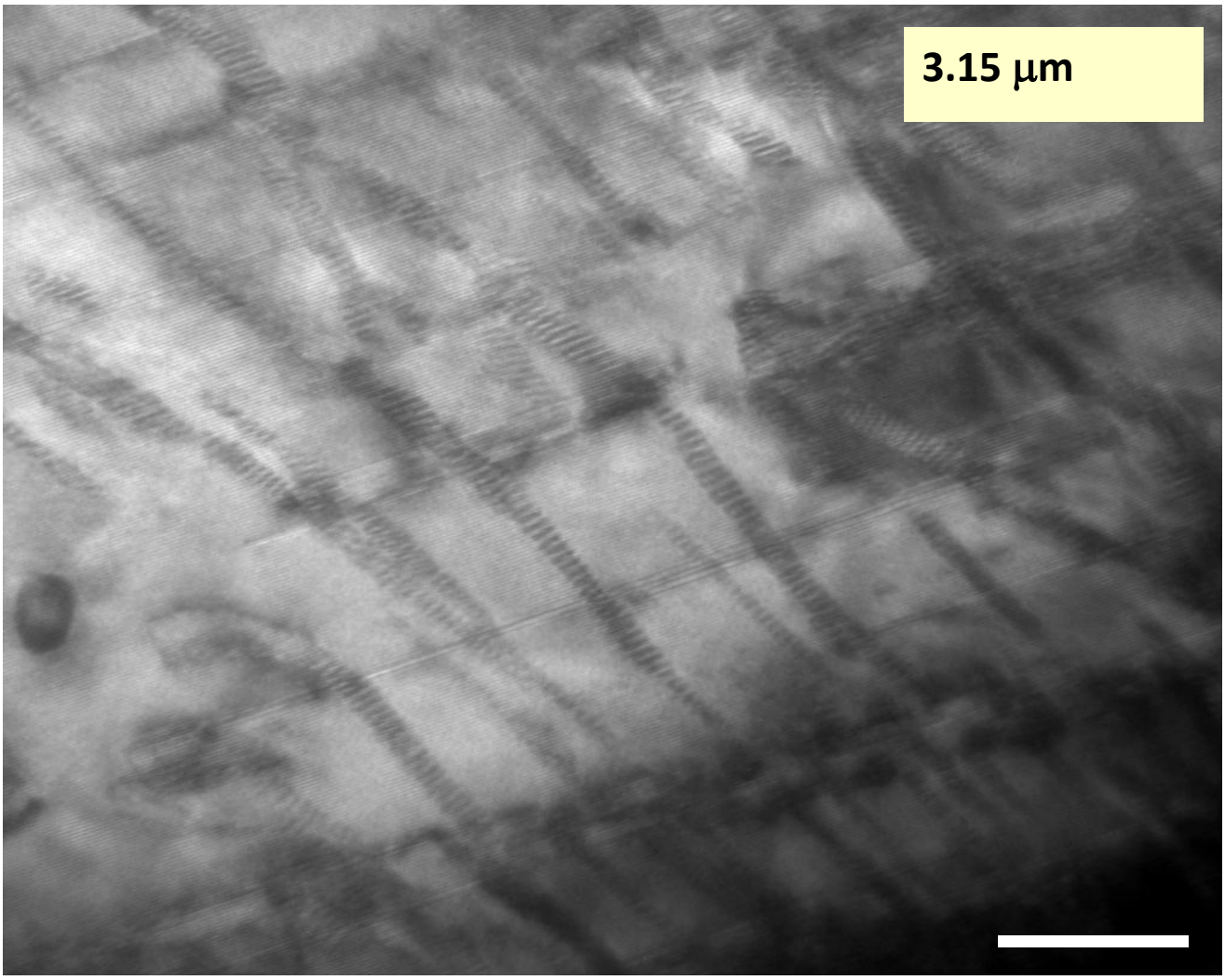

Figure 31: A TEM image of a sample showing BZO columnar defects and well as more isotropic disorder that is rare earth second-phase oxide materials.

temperatures would be very similar to the sample that is dominated by BSO columnar defects, but due to the splay in the columnar defects the angular current density profile will have a much broader peak. These features are indeed observed in measurements at T = 65 K shown in figure 32. It is also evident at low magnetic fields that there is an upturn in the J_c near the *ab*-plane, which can be attributed to some layering of the RE-oxide precipitates, combined with effects of mass anisotropy like those observed with isotropic defects in case II.

There are many other curious features in the angular J_c of this mixed pinning landscape. At low magnetic fields, the peak is very far away from the ~6° average tilt that the columnar defects have, relative to the sample normal. In fact, the peak in J_c actually occurs at angles as high as ~20°. As the applied magnetic field is increased, the peak shifts in position and eventually occurs at ~6°. This phenomenon can be seen in figure 33. What is being articulated in figure 33 is a misalignment between the applied magnetic field and the internal magnetic field. Conceptually, one expects the J_c to be largest when the *internal* field (vortices) is parallel to the columnar defects. The misalignment between internal and external field directions is probably due to a competition between the geometry effects of a flat, planar sample and the intrinsic superconductive anisotropy of the material; there are, however, further complicating factors including the presence of isotropic pinning centers.

There is an approximate scaling that occurs with this peak position. Assuming that columnar defects act as passive detectors of the internal field direction, Silhanek et al. developed a scaling relation using minimization of the equilibrium energy in the

presence of geometric effects and the material anisotropy of the cuprate superconductor[44]. The resulting scaling has a peak shift that is inversely proportion to the reduced magnetic field $h = H/H_{c2}$.

An approximate scaling of the peak position with h^{-1} can be seen in figure 34. This phenomenon holds over a fairly large range of temperatures, though there does seem to be deviation away from linearity at low magnetic fields where the material becomes highly irreversible magnetically. The model relation of Silhanek et al. can be fit to (nearly) linear data in figure 34, where the slope depends in the theory on a small number of superconductive parameters of the cuprate. Interpreting the observed slope in terms of the Ginzburg-Landau parameter yields a very small value, $\kappa \approx 3$, compared with experimental values of ~100. Qualitatively, the added pinning due to precipitates, combined with their layering near the *ab*-planes, complicates the pinning landscape and tends to shift the peak in J_c away from the *c*-axis. This mimics the effect of a small value for κ in the theory. However, given that the pinning landscape is far more complex than that treated in the theory of Silhanek et al., this analysis will not be pursued further.

At low temperatures, the angular dependence of J_c with the mixed pinning landscape is similar to that of the other two pinning landscapes, cases I and II. Much like the previous two pinning landscapes at 5 K, the current density profile has no observed angular selectivity present. This is apparent in figure 35. While the observed properties at 5 K are similar in many regards to those in case I (dominated by columnar defects), the mixed pinning landscape exhibits an upturn in the current density profile as the *ab*-plane is approached. However, the most interesting difference in the mixed pinning landscape appears at intermediate temperatures. As can be seen in the current density

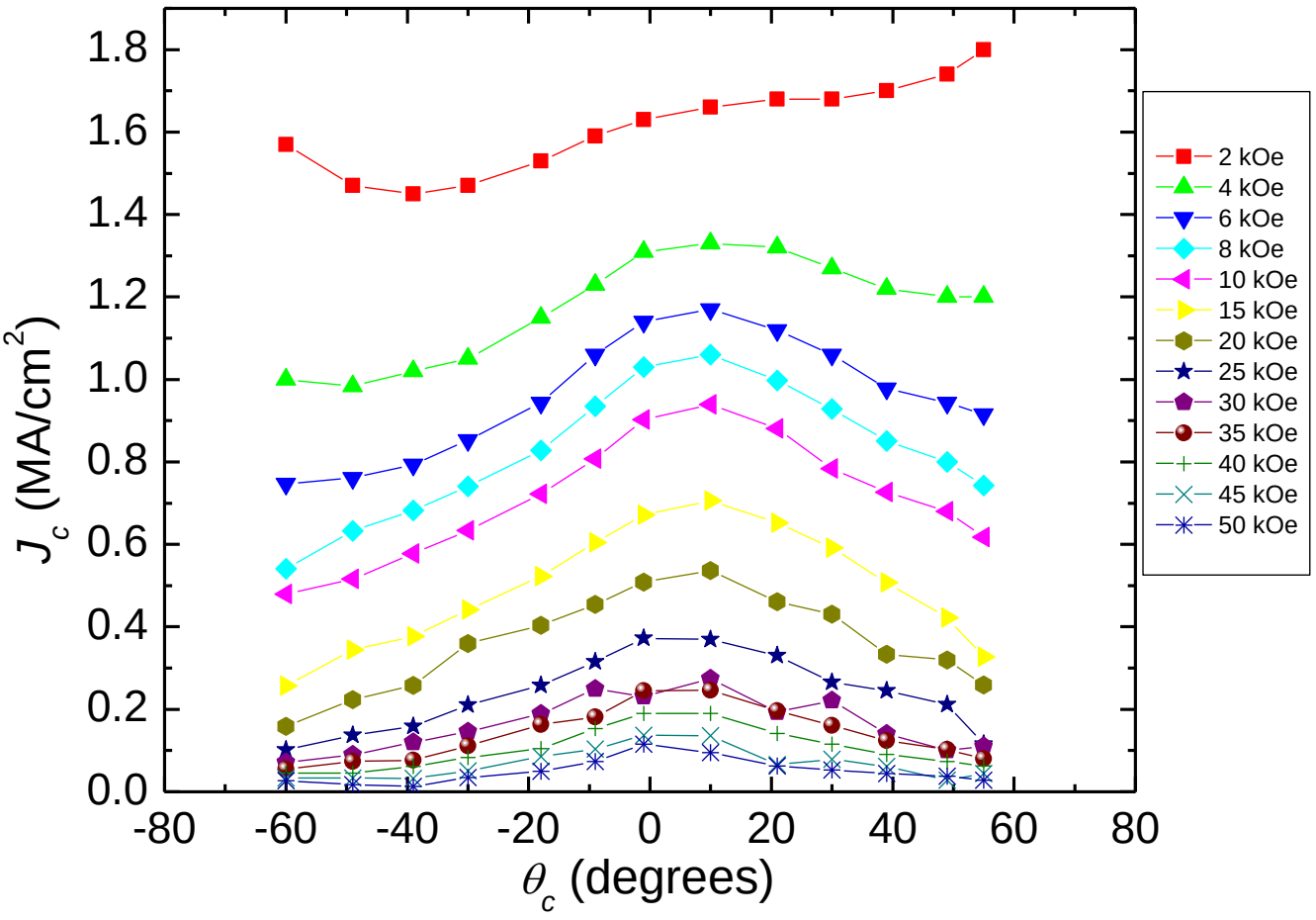

Figure 32**: The mixture of defects and splay in the BZO columnar defects produces a wider peak. Also there is an upturn in the current density near the *ab*-plane at low magnetic fields. Here *T* = 65 K data are shown.**

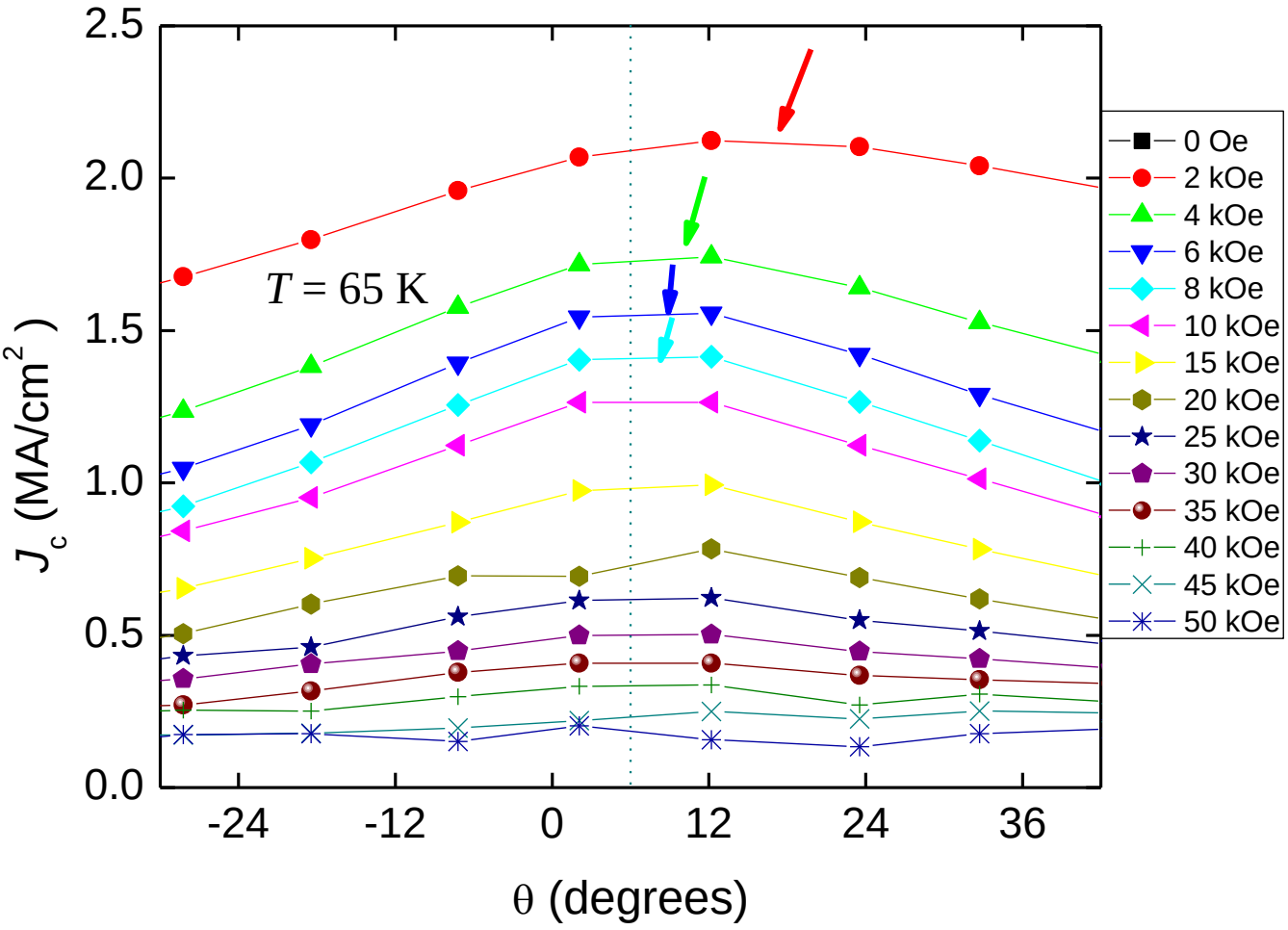

Figure 33: The peak in the mixed sample moves as a function of applied magnetic field. This occurs due to a mismatch between the internal magnet field and the applied *H* field.

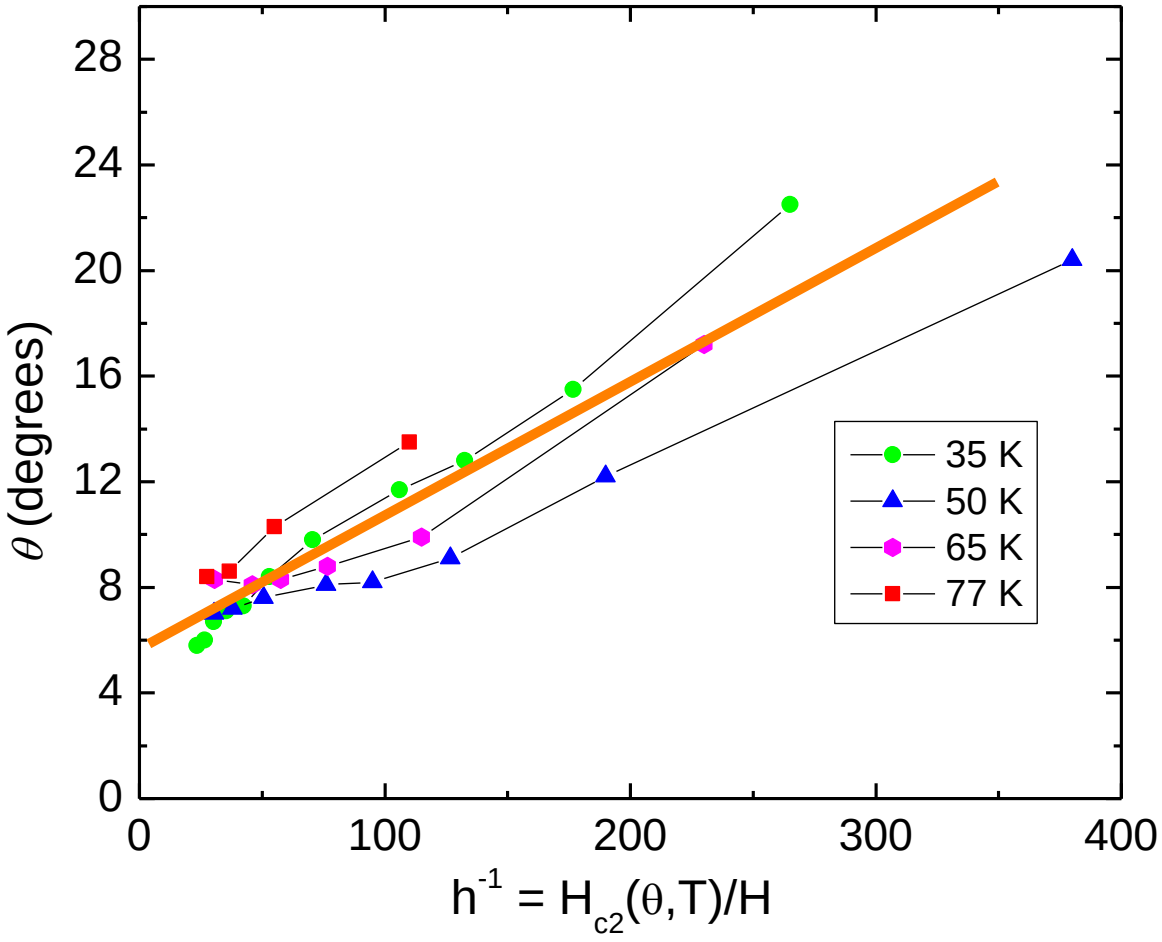

Figure 34: A scaling of the peak position in J_c versus reduced magnetic field. When the magnetic field becomes large enough, the peak position coincides with the ~6 degree tilted orientation at which the columns grew.

profiles in figure 36, there is a very clear evolution from low magnetic field curves that have no angular selectivity to high magnetic field curves that show some angular selectivity near the *c*-axis. At this intermediate temperature, a clear pattern appears that has been seen often in this study appears: a dominance of strong or columnar defects at high temperatures and high magnetic fields, while at low temperatures and low magnetic fields weak isotropic pinning seems to dominate. Clearly there is more in play than just simple anisotropy and geometry effects as incorporated in the model of Silhanek et al., making clear why the parameters may not make physical sense.

Untangling the Pinning Landscape

The dominant two distinct types of pinning that are present in this material are isotropic pinning and strong columnar pinning. As described in chapter 2, Plain et al. provide an interesting way to try and untangle weak and strong types of pinning[20]. By using equation 2.11 and fitting the temperature dependence of the J_c at constant magnetic fields, one can attempt to determine which type of pinning is dominant. When using equation 2.11, it is important to remember that the weak pinning terms are related to isotropic point-like pinning defects and the strong terms are associated with large, extended defect centers. This equation was developed for a magnetic field that is parallel to the *c*-axis and that is the configuration in which all measurements were made for this analysis.

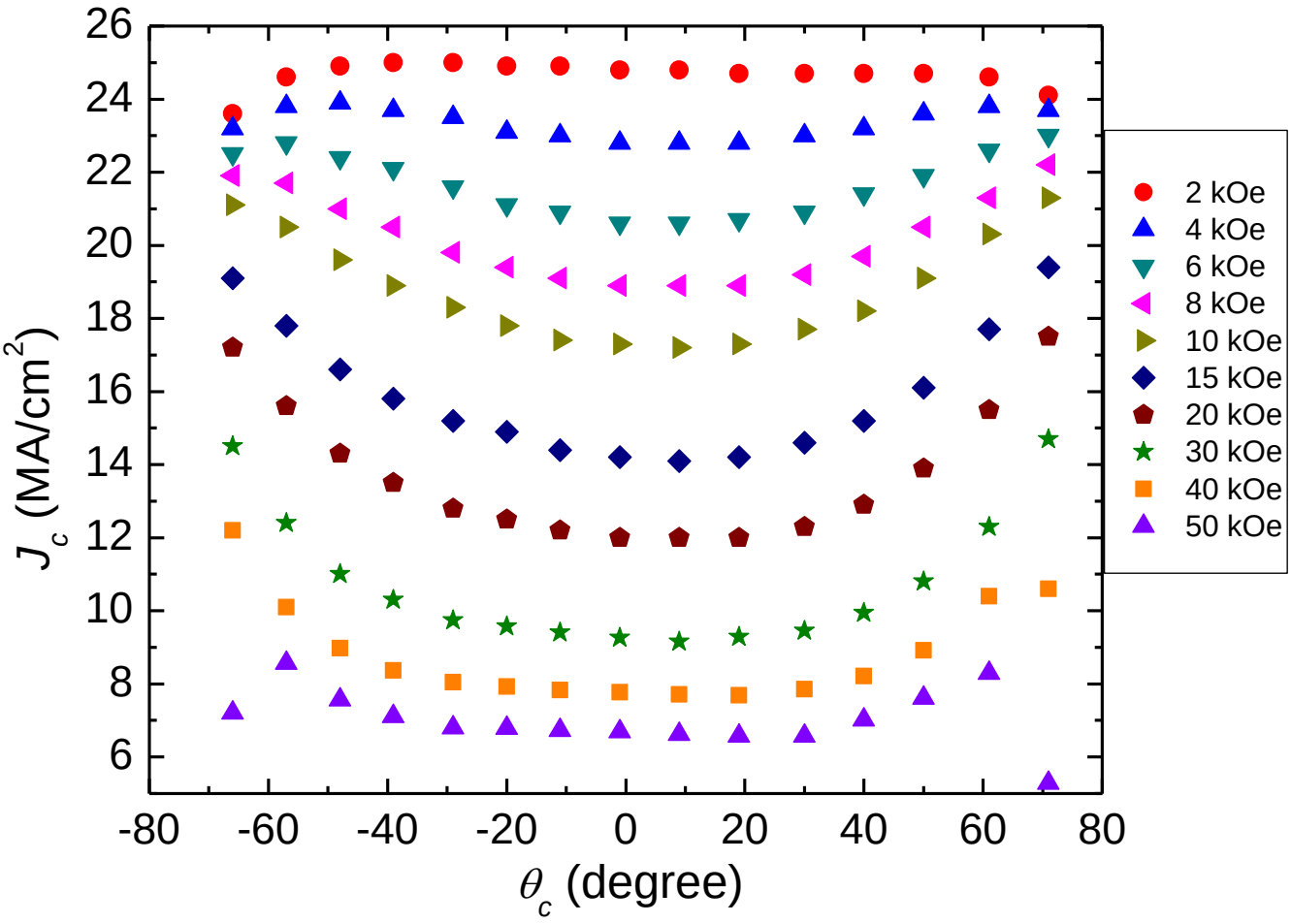

Figure 35: Current density J_c for mixed pinning landscape at 5 K. The angular selectivity seems to once again be washed out at all applied magnetic fields at low temperatures.

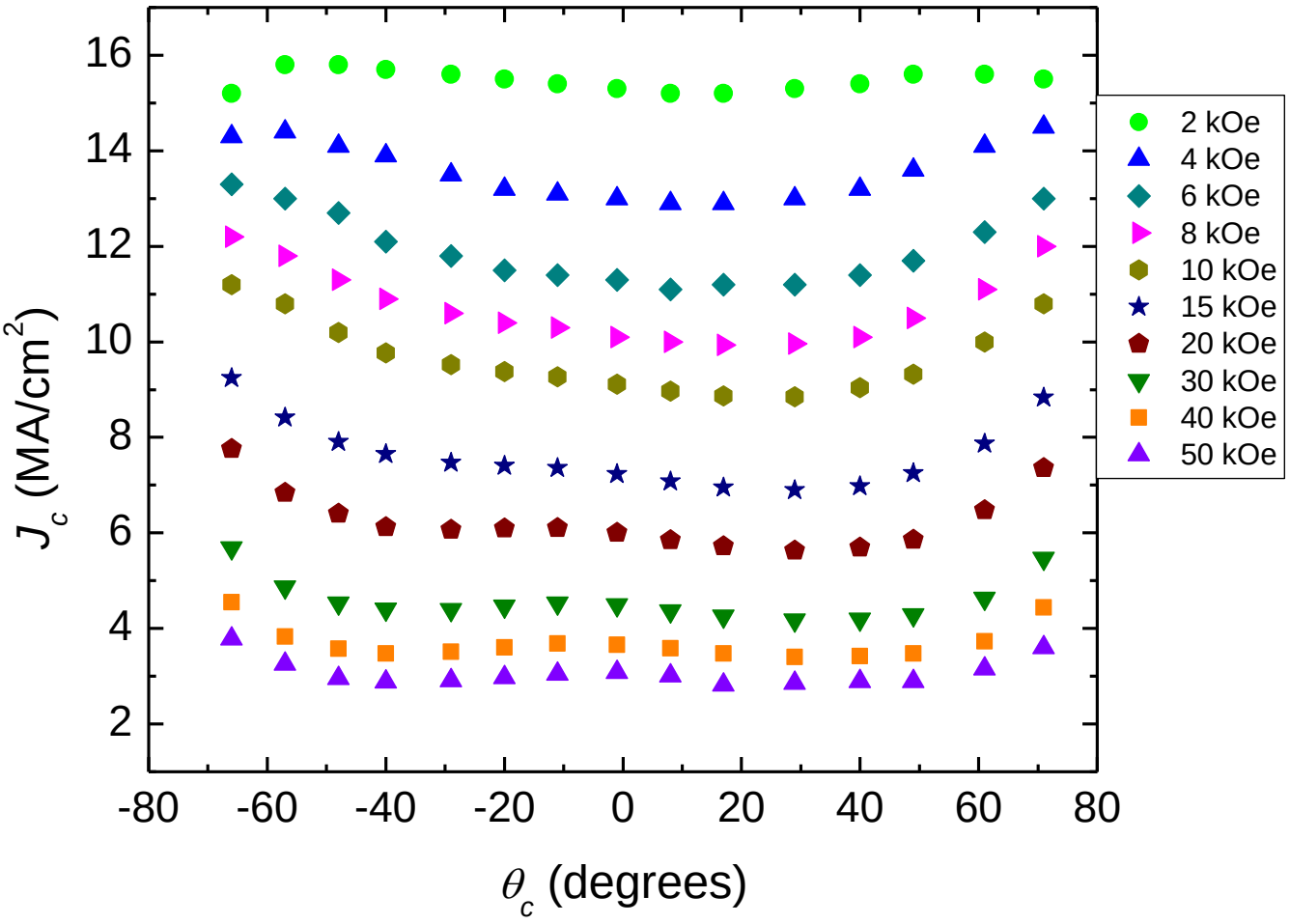

Figure 36: Current density J_c for mixed pinning landscape at 20 K. At this intermediate temperature, there is a clear competition between the different types of pinning. At the highest magnetic fields, there is some angular selectivity present, but as the magnetic field is reduced, the angular selectivity is washed out.

Figure 37 shows the fit to the equation 2.11 for experimental data $J_c(T)$ with an applied magnetic field of 1 T. It is clear from this figure that at high temperatures, strong pinning from columnar defect pinning and large sparse defects dominates the pinning landscape. It is also obvious that at lower temperatures, weak pinning from point-like defects becomes progressively more significant until finally there is a crossover to a regime in which weak pinning dominates. Below ~10 K, the isotropic pinning centers become the dominant type of pinning. This interpretation is corroborated by the angular current density profiles that show the lack of angular selectivity at low temperatures and at relatively low magnetic fields.

The next obvious investigation is to increase the magnetic field and determine how a larger magnetic field affects the relative contributions to the pinning and this crossover temperature. Thus a similar analysis was made for the temperature dependence of the mixed defect sample in a field of 3 T. The results in figure 38 show that at this higher magnetic field, the strong pinning contribution dominates over all of the achievable temperature range. If extrapolated, the two terms in Eq. 2.11 do eventually cross, but only below the base temperature on the magnetometer. Once again this paints a self-consistent picture with the angular current density profiles.

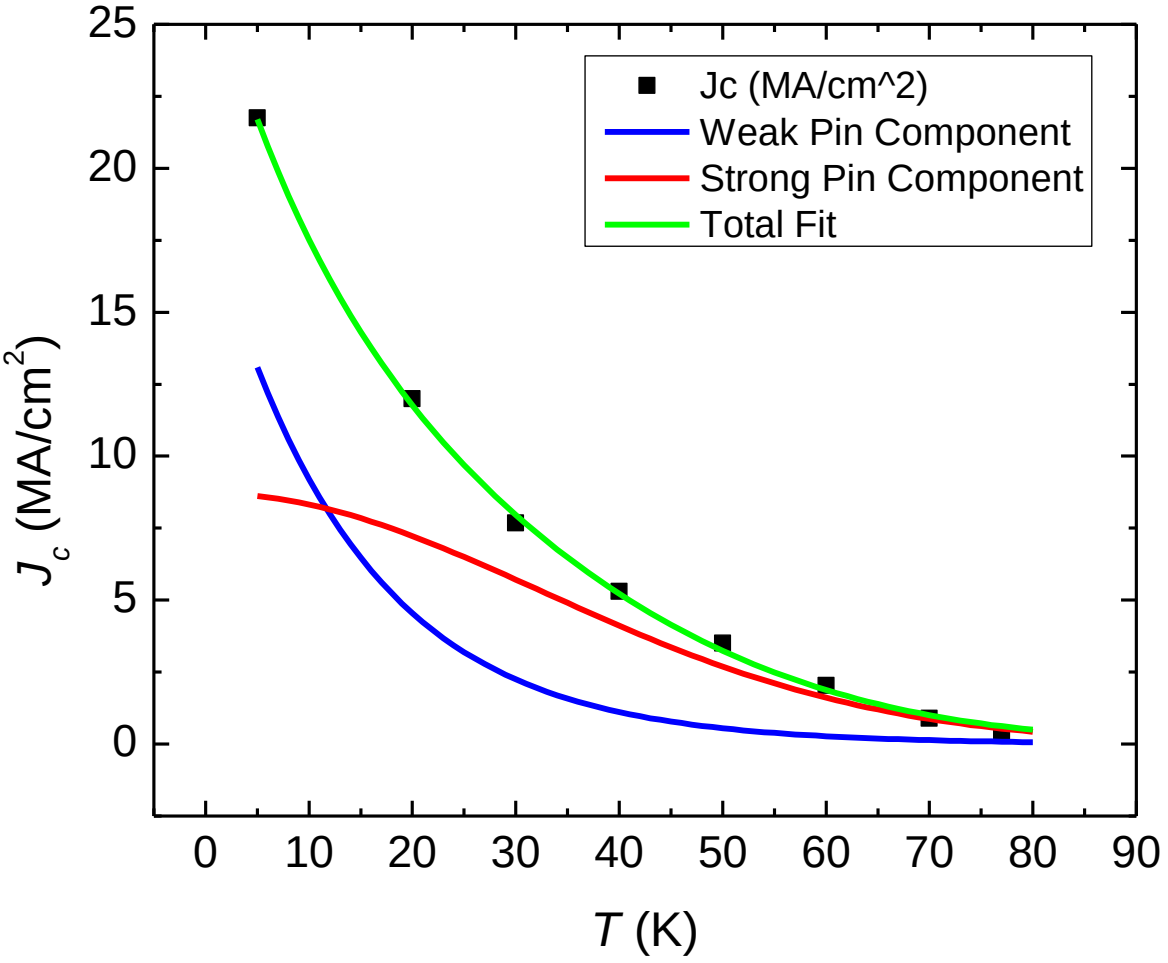

Figure 37: The mixed pinning landscape sample's temperature evolution of J_c at an applied magnetic field of 1 T. At high temperatures, strong defects dominate the pinning landscape. Below ~10 K, there is a crossover between the dominance of strong and weak defects, producing a consistent picture with the angular current density profiles.

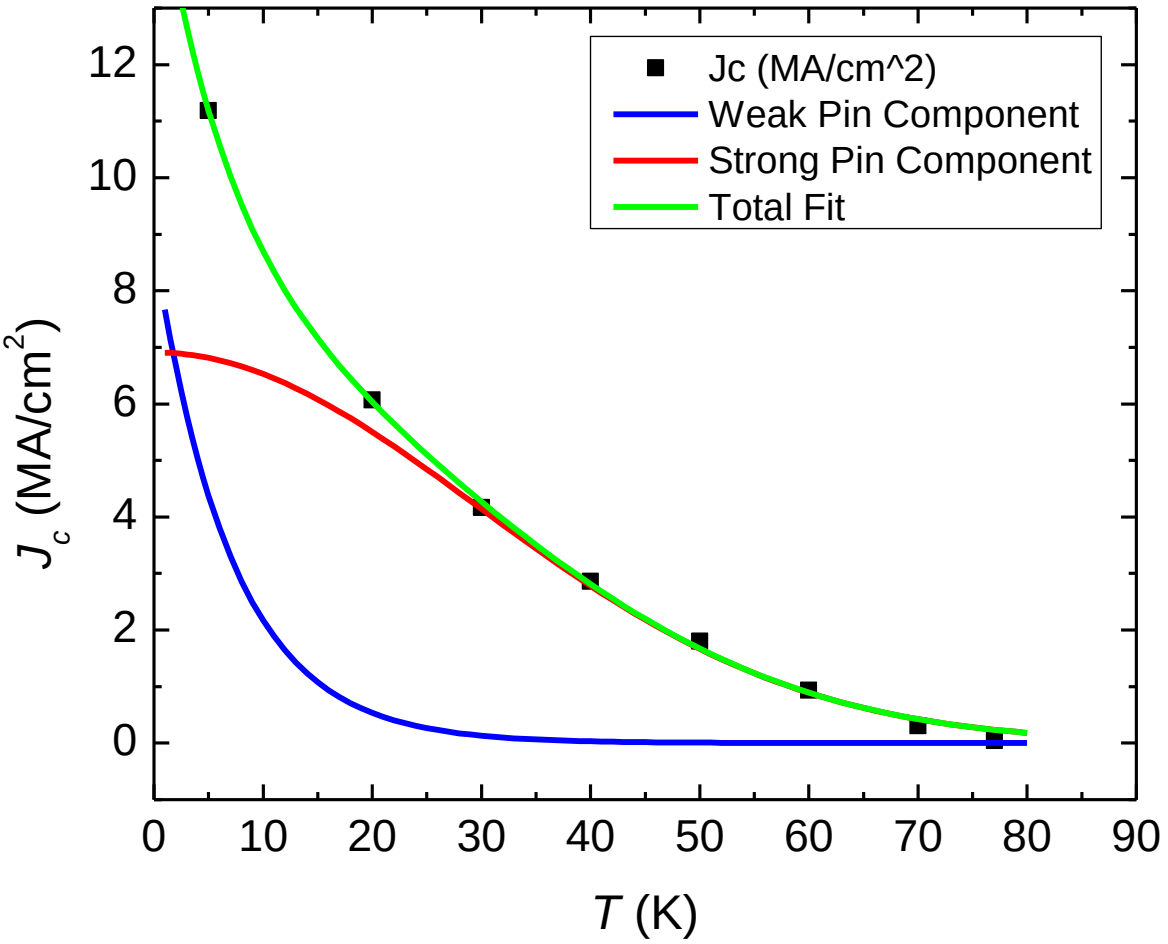

Figure 38: The mixed pinning landscape sample's temperature evolution of J_c at an applied magnetic field of 3 T. Here strong pinning seems to dominant over the entire temperature range. This is also consistent with the angular current density profiles.

Conclusions

The complexity in the pinning landscape of modern coated conductors is most evident in this sample. Its current density profiles have some features that are similar to the earlier cases I or II dominated mostly by columnar or isotropic defects alone, while some other features are distinctly different. The tilt and splay of the columnar defects alone drastically change the current density profiles of the mixed defect sample, compared to that with columnar defects. The Plain analysis for the present sample is consistent with its angular current density profiles as well. Figure 39 shows the angular J_c of the mixed pinning sample at various temperatures and at 1 T and 3 T. It is plotted as linear and semi-log plots side by side to show the absolute and fractional variations, respectively. As is clear from this figure, the current density profiles show a nice picture where at low temperatures and fields, pinning by isotropic defects is dominant, while at high temperatures and magnetic fields, the pinning is angularly selective due to the columnar defects.

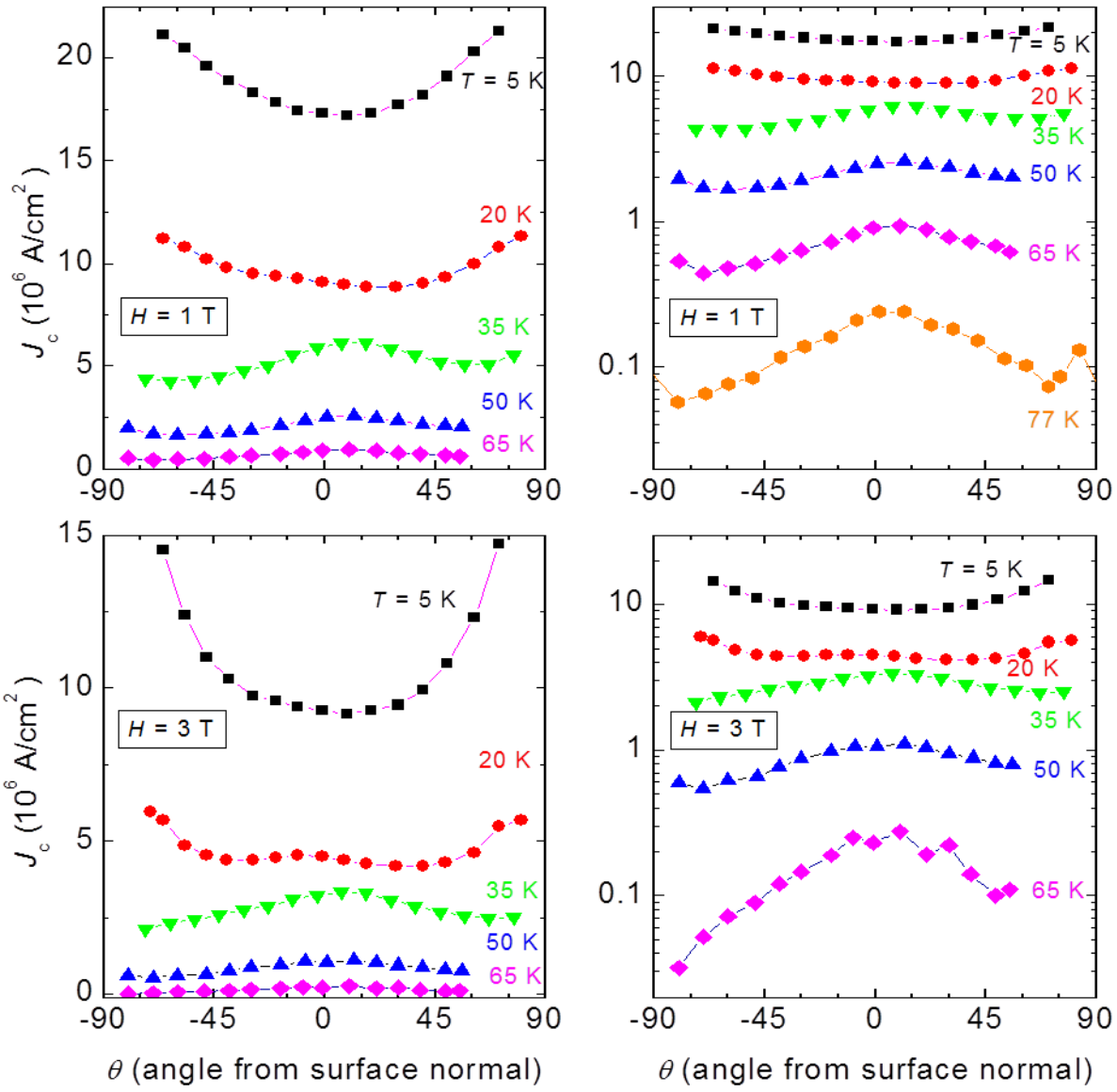

Figure 39: Angular current density profiles of the mixed pinning sample plotted on both linear and semi-log axes. The figure clearly shows the evolution between angular selectivity at high magnetic fields and temperatures to the pinning of low temperatures and fields where the angular variation reflects that of isotropic pins.

7 CONCLUSIONS

The ability to make contact-free measurements of the critical current density profiles, i.e., versus magnetic field orientation, is an important new tool that was used to study three distinct pinning landscapes. The ability to measure samples over large temperature ranges without the hazard of destroying them is not only useful for basic vortex physics, but it also produces useful information for applications of superconducting wires as well. This new tool used in conjunction with some traditional magnetic methods for studying superconductors has provided a new and self-consistent picture of competition between different types of pinning.

By examining and contrasting the α-values of samples dominated by both columnar defects and large sparse defects, matching field effects were seen in cuprates with self-assembled columnar defects. The ability to measure the current density of the material over a large temperature range gives confidence that geometric matching is occurring in the material with BSO columnar defects, case I. This phenomenon appears to disappear at low temperatures, which is consistent with the results from the angular critical current density profiles. This phenomenon also appears to exist in the α values for the sample dominated by columnar defects. The extra J_c that the matching effects produce at high temperatures is reflected in the suppression of the α values at high temperatures. As the temperature is reduced, however, the α values increase to values in the range of 1/2-5/8, as predicted theoretically for materials dominated by isotropic pins. Experimental studies of a sample dominated by isotropic defects (case II) yielded values lying in this range, confirming the emerging importance of isotropic pins at low temperatures, even in the columnar-defected material.

Finally a sample with a mixture of columnar defects and isotropic rare earth-oxide precipitates was studied, which proved to form a complex pinning landscape. The temperature and orientation dependence of its critical current density J_c exhibits some features similar to those observed with the simpler defect landscapes, cases I and II. This mixed sample also showed an interesting difference between the internal and external magnetic field directions, which was observable due to the tilting of the columns in the sample.

In conclusion, a qualitatively consistent picture arises, which a varying mixture of strong and weak pinning effects as proposed by Plain et al. Also there is a competition between angularly selective and nonselective pinning. These effects change not only the angular critical current density profiles, but also the dependence on magnetic field (the α-values) and perhaps the observability of matching field effects.

LIST OF REFERENCES

[1] H. K. Onnes, Proceedings of the Koninklijke Akademie Van Wetenschappen Te Amsterdam **14**, 113 (1911).
[2] J. G. Bednorz and K. A. Muller, Zeitschrift Fur Physik B-Condensed Matter **64**, 189 (1986).
[3] Y. Kamihara, T. Watanabe, M. Hirano, and H. Hosono, Journal of the American Chemical Society **130**, 3296 (2008).
[4] Y. Iijima, N. Tanabe, O. Kohno, and Y. Ikeno, Applied Physics Letters **60**, 769 (1992).
[5] Y. Y. Xie, et al., Physica C-Superconductivity and Its Applications **426**, 849 (2005).
[6] W. Meissner and R. Ochsenfeld, Naturwissenschaften **21**, 787 (1933).
[7] F. London and H. London, Proceedings of the Royal Society of London Series A-Mathematical and Physical Sciences **149**, 0071 (1935).
[8] V. Ginzburg and L. Landau, Zh. Eksp. Teor. Fiz., 1950), Vol. 20, p. 1064.
[9] A. A. Abrikosov, Soviet Physics JETP-USSR **5**, 1174 (1957).
[10] I. Maggioaprile, C. Renner, A. Erb, E. Walker, and O. Fischer, Physical Review Letters **75**, 2754 (1995).
[11] G. Blatter, M. V. Feigelman, V. B. Geshkenbein, A. I. Larkin, and V. M. Vinokur, Reviews of Modern Physics **66**, 1125 (1994).
[12] M. Konczykowski, F. Rullieralbenque, E. R. Yacoby, A. Shaulov, Y. Yeshurun, and P. Lejay, Physical Review B **44**, 7167 (1991).
[13] L. Krusin-Elbaum, J. R. Thompson, R. Wheeler, A. D. Marwick, C. Li, S. Patel, and D. T. Shaw, Applied Physics Letters **64**, 3331 (1994).
[14] A. Goyal, et al., Superconductor Science & Technology **18**, 1533 (2005).
[15] S. Kang, et al., Science **311**, 1911 (2006).
[16] Y. Bugoslavsky, L. F. Cohen, G. K. Perkins, M. Polichetti, T. J. Tate, R. Gwilliam, and A. D. Caplin, Nature **411**, 561 (2001).
[17] G. Blatter, V. B. Geshkenbein, and A. I. Larkin, Physical Review Letters **68**, 875 (1992).
[18] P. W. Anderson, Physical Review Letters **9**, 309 (1962).
[19] P. W. Anderson and Y. B. Kim, Reviews of Modern Physics **36**, 39 (1964).
[20] J. Plain, T. Puig, F. Sandiumenge, X. Obradors, and J. Rabier, Physical Review B **65**, 10452 (2002).
[21] B. D. Josephson, Physics Letters **1**, 251 (1962).
[22] C. P. Bean, Reviews of Modern Physics **36**, 31 (1964).
[23] W. A. Fietz and W. W. Webb, Physical Review **178**, 657 (1969).
[24] A. M. Campbell and J. E. Evetts, Advances in Physics **21**, 199 (1972).
[25] O. Polat, J. W. Sinclair, Y. L. Zuev, J. R. Thompson, D. K. Christen, S. W. Cook, D. Kumar, Y. M. Chen, and V. Selvamanickam, Physical Review B **84**, 024519 (2011).
[26] J. R. Thompson, O. Polat, D. K. Christen, D. Kumar, P. M. Martin, and J. W. Sinclair, Applied Physics Letters **93**, 042506 (2008).

[27] L. Pust, J. Kadlecova, M. Jirsa, and S. Durcok, Journal of Low Temperature Physics **78**, 179 (1990).
[28] M. P. Maley, J. O. Willis, H. Lessure, and M. E. McHenry, Physical Review B **42**, 2639 (1990).
[29] E. M. Gyorgy, R. B. Vandover, K. A. Jackson, L. F. Schneemeyer, and J. V. Waszczak, Applied Physics Letters **55**, 283 (1989).
[30] C. V. Varanasi, J. Burke, L. Brunke, H. Wang, M. Sumption, and P. N. Barnes, Journal of Applied Physics **102**, 063909 (2007).
[31] C. V. Varanasi, J. Burke, H. Wang, J. H. Lee, and P. N. Barnes, Applied Physics Letters **93**, 092501 (2008).
[32] G. S. Mkrtchya and V. V. Shmidt, Soviet Physics Jetp-Ussr **34**, 195 (1972).
[33] O. Daldini, P. Martinol, J. L. Olsen, and G. Berner, Physical Review Letters **32**, 218 (1974).
[34] P. Martinoli, Physical Review B **17**, 1175 (1978).
[35] M. Baert, V. V. Metlushko, R. Jonckheere, V. V. Moshchalkov, and Y. Bruynseraede, Physical Review Letters **74**, 3269 (1995).
[36] J. I. Martin, M. Velez, J. Nogues, and I. K. Schuller, Physical Review Letters **79**, 1929 (1997).
[37] A. Castellanos, R. Wordenweber, G. Ockenfuss, A. VonderHart, and K. Keck, Applied Physics Letters **71**, 962 (1997).
[38] Y. Zhang, et al., Applied Physics Letters **98**, 042509 (2011).
[39] C. J. van der Beek, M. Konczykowski, A. Abal'oshev, I. Abal'osheva, P. Gierlowski, S. J. Lewandowski, M. V. Indenbom, and S. Barbanera, Physical Review B **66**, 024523 (2002).
[40] V. Vinokur, B. Khaykovich, E. Zeldov, M. Konczykowski, R. A. Doyle, and P. H. Kes, Physica C **295**, 209 (1998).
[41] D. R. Nelson and V. M. Vinokur, Physical Review B **48**, 13060 (1993).
[42] J. R. Thompson, J. W. Sinclair, D. K. Christen, Y. F. Zhang, Y. L. Zuev, C. Cantoni, Y. M. Chen, and V. Selvamanickam, Superconductor Science & Technology **23**, 014002 (2010).
[43] B. Maiorov, S. A. Baily, H. Zhou, O. Ugurlu, J. A. Kennison, P. C. Dowden, T. G. Holesinger, S. R. Foltyn, and L. Civale, Nature Materials **8**, 398 (2009).
[44] A. V. Silhanek, L. Civale, and M. A. Avila, Physical Review B **65**, 174525 (2002).

VITA

John Sinclair was born in South Bend IN. After graduating from undergraduate school at the University of Tennessee Knoxville, he began his graduate work there working with Dr. Jim Thompson, preforming most of his experimental work at Oak Ridge National Laboratories. He received the honor of joining Sigma Pi Sigma and Phi Beta Kappa in undergraduate school, as well as a Chancellors Certificate of Academic Excellence and the Undergraduate Research Award from the Physics department at the University of Tennessee.